저작자표시-비영리-변경금지 2.0 대한민국

이용자는 아래의 조건을 따르는 경우에 한하여 자유롭게

- 이 저작물을 복제, 배포, 전송, 전시, 공연 및 방송할 수 있습니다.

다음과 같은 조건을 따라야 합니다:

저작자표시. 귀하는 원저작자를 표시하여야 합니다.

비영리. 귀하는 이 저작물을 영리 목적으로 이용할 수 없습니다.

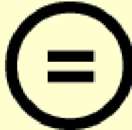
변경금지. 귀하는 이 저작물을 개작, 변형 또는 가공할 수 없습니다.

- 귀하는, 이 저작물의 재이용이나 배포의 경우, 이 저작물에 적용된 이용허락조건을 명확하게 나타내어야 합니다.
- 저작권자로부터 별도의 허가를 받으면 이러한 조건들은 적용되지 않습니다.

저작권법에 따른 이용자의 권리는 위의 내용에 의하여 영향을 받지 않습니다.

이것은 이용허락규약(Legal Code)을 이해하기 쉽게 요약한 것입니다.

Disclaimer

dCollection

이학박사 학위논문

Synthesis of large monolayer MoS_2 film and its application to field-effect transistors

대면적 단분자층 이황화 몰리브덴 박막 합성 및 전계효과 트랜지스터에의 응용

2017 년 8 월

서울대학교 대학원

물리천문학부

김 태 영

Synthesis of large monolayer MoS_2 film and its application to field-effect transistors

지도 교수 이 탁 희

이 논문을 이학박사 학위논문으로 제출함
2017 년 6 월

서울대학교 대학원
물리천문학부
김 태 영

김태영의 이학박사 학위논문을 인준함
2017 년 6 월

위 원 장 ________ 차 국 린 ________ (인)

부위원장 ________ 이 탁 희 ________ (인)

위 원 ________ 박 제 근 ________ (인)

위 원 ________ 민 홍 기 ________ (인)

위 원 ________ 이 관 형 ________ (인)

Abstract

Department of Physics and Astronomy

Doctor of Philosophy

Synthesis of large monolayer MoS_2 film and its application to field-effect transistors

Tae-Young Kim

Two-dimensional (2D) transition-metal dichalcogenides (TMDCs) have gained considerable attention as an emerging semiconductor due to their promising atomically thin film characteristics with good field-effect mobility and a tunable bandgap energy. Among TMDC materials, molybdenum disulfide (MoS_2) has gained significant attention due to its direct bandgap of 1.8 eV as a single layer. Herein, numerous studies have explored the application of MoS_2 in nanoelectronic devices. To make full use of its unique optical and electrical merits in practical applications, however, synthesis of large and uniform monolayer MoS_2 is highly necessary. In this regard, a chemical vapor deposition (CVD) technique has been intensively used to produce large and uniform monolayer MoS_2.

Meanwhile, their electronic applications have been generally realized with conventional inorganic electrodes and dielectrics implemented using conventional photolithography or transferring processes that are not compatible with large-area and flexible device applications. To facilitate the advantages of 2D TMDCs in practical applications, novel strategies for realizing flexible and transparent 2D electronics using low-temperature, large-area, and low-cost processes should be developed. Here, in this dissertation, the study on the atomically thin MoS_2 synthesis and its application to FETs will be discussed.

First, the effect of irradiation on MoS_2 FETs with 10 MeV high energy proton beams will be discussed. The electrical characteristics of the devices were measured before and after proton irradiation with different fluence conditions. The electrical changes were explained by the proton-irradiation-induced traps, including positive

oxide-charge traps in the SiO_2 layer and trap states at the interface between the MoS_2 channel and the SiO_2 layer.

Second, the CVD synthesis of large and monolayer MoS_2 film will be discussed. The predominantly monolayer character of the CVD-grown MoS_2 film was verified by atomic force microscopy (AFM), Raman, and photoluminescence (PL) spectroscopy measurements.

Third, the electrical properties of synthesized large-area monolayer MoS_2 field-effect transistors with low-cost inkjet-printed Ag electrodes will be discussed. The monolayer MoS_2 film was grown by CVD method, and the top-contact Ag source/drain electrodes (*S/D*) were deposited onto the films using a low-cost drop-on-demand inkjet-printing process without any masks and surface treatments. The electrical characteristics of FETs were comparable to those fabricated by conventional deposition methods such as photo or electron beam lithography.

Last, the fully printed transparent CVD-synthesized monolayer MoS_2 phototransistor arrays on flexible polymer substrates will be discussed. All the electronic components, including dielectric and electrodes, were directly deposited with mechanically tolerable organic materials by inkjet-printing technology onto transferred monolayer MoS_2. By integrating the soft organic components with ultra-thin MoS_2, the fully printed MoS_2 phototransistors exhibits excellent transparency and mechanically stable operation.

Keyword : MoS_2, field-effect transistor, electrical characteristics, chemical vapor synthesis
Student Number : 2013-30113

Table of Contents

Abstract i

Table of Contents iii

List of Figures vi

Chapter 1. Introduction

1.1. Graphene and 2D materials 1

1.2. Molybdenum disulfide (MoS_2) 1

References 2

Chapter 2. Proton beam irradiation effect on atomically thin MoS_2 field-effect transistors

2.1. Introduction 3

2.2. Experiments 4

2.2.1. Device fabrication process 4

2.2.2. Proton beam irradiation experiment 6

2.2.3. Electrical characteristics measurements 6

2.3. Results and discussions 6

2.3.1. Electrical characteristics 6

2.3.2. Dose-dependence and Raman spectra.. 9

2.3.3. Time-dependence 11

2.3.4. Stopping and Range of Ions in Matter 12

2.3.5. Energy band diagram 14

2.4. Conclusion 15

References 16

Chapter 3. Chemical vapor deposition of monolayer MoS_2 film

3.1. Introduction 20

3.1.1. Limit of mechanical exfoliation 20

3.1.2. Many synthesis methods 20

3.2. CVD system setup 21
3.3. Material characterization 22
3.3.1. Atomic force microscopy 22
3.3.2. Raman and photoluminescence 23
3.3.3. Electrical characteristics of triangular islands 24
3.4. Conclusion 25
References 26

Chapter 4. Inkjet-printed contact electrodes on CVD-synthesized MoS_2 film

4.1. Introduction 29
4.2. Experiments 31
4.2.1. Inkjet-printing process 32
4.3. Results and discussions 32
4.3.1. Electrical characteristics 32
4.3.2. Y-function method and contact resistances 33
4.3.3. Electrical instability and gate-bias stress effect 35
4.4. Conclusion 37
References 38

Chapter 5. Fully flexible and transparent MoS_2 phototransistor with inkjet-printed components

5.1. Introduction 43
5.2. Experiments 44
5.2.1. Device fabrication process 44
5.2.2. Light illumination setup 45
5.2.3. Optical transmittance of the device 47
5.3. Results and discussions 48
5.3.1. Fully-printed MoS_2 phototransistors 48
5.3.2. Characteristics of CVD-grown monolayer MoS_2 film 49

5.3.3. Electrical characteristics under bent conditions ………………... 52
5.3.4. Photo-characteristics ……………………………………………... 53
5.4. Conclusion ……………………………………………………………. 56
References …………………………………………………………...… 57

Chapter 6. Summary

Abstract (In Korean) …………………………………………………………… 61
Curriculum Vitae ………………………………………………………….…. 63
Acknowledgement (감사의 글) ………………………………………………... 68

List of Figures

Figure 2.1 Schematic illustration of device fabrication process. Adapted from Kim *et al.*

Figure 2.2 (a) Optical images showing the fabrication of a MoS_2 FET device. (b) Schematic illustration of proton beam irradiation on a MoS_2 FET device. (c) AFM image of the MoS_2 FET device with a cross-sectional topographic profile indicated by the blue line (MoS_2 flake). Red dashed-lines in (a) and (c) indicate MoS_2 flakes. Adapted from Kim *et al.*

Figure 2.3 Representative electrical characteristics of MoS_2 FET devices. (a) Before and (b) after proton irradiation with a beam fluence of 10^{12} cm^{-2}. (c) Before and (d) after proton irradiation with a fluence of 10^{14} cm^{-2}. (a, c) Output characteristics (I_{DS}–V_{DS}) measured for different gate voltages. (b, d) Transfer characteristics (I_{DS}–V_{GS}) measured at a fixed V_{DS} = 0.5 V. The inset figures of (b) and (d) are the transfer characteristics on a log scale. Adapted from Kim *et al.*

Figure 2.4 Representative electrical characteristics of a MoS_2 FET device before and after proton irradiation with a beam fluence of 10^{13} cm^{-2} (corresponding to an irradiation time of 200 sec). (a) I_{DS}–V_{DS} curves measured for different gate voltages before (left) an d after (right) proton irradiation. (b) I_{DS}–V_{GS} curves measured at a fixed V_{DS} = 0.5 V before (open circles) and after (filled circles) proton irradiation. Adapted from Kim *et al.*

Figure 2.5 Statistical data for the (a) normalized conductance, (b) normalized current, and (c) change in the threshold voltage of the devices following proton irradiation with different beam fluences (10^{12}, 10^{13}, and 10^{14} cm^{-2}). Raman spectra of MoS_2 flakes before and after proton beam irradiation with the fluences of (d) $\Phi = 10^{12}$ cm^{-2} and (e) $\Phi = 10^{14}$ cm^{-2}. (f) Schematic illustrations of MoS_2 vibration modes. Adapted from Kim *et al.*

Figure 2.6 Time-dependence of the I_{DS}–V_{GS} curves of the MoS_2 FET devices before proton irradiation and 1, 3, and 5 days after proton irradiation with fluences of (a) 10^{12} cm^{-2}, (b) 10^{13} cm^{-2}, and (c) 10^{14} cm^{-2}. The (d) normalized current, (e) normalized conductance and (f) change in the threshold voltages of the devices are plotted as a function of time (i.e., before proton irradiation and at 1, 3, and 5 days after proton irradiation) for the three different fluence conditions of 10^{12}, 10^{13}, and 10^{14} cm^{-2}.

Adapted from Kim *et al.*

Figure 2.7 Energy loss depth profiles of irradiated protons calculated using SRIM. The inset image is a zoomed plot for the energy loss depth profile in the range of 0–400 nm from the top surface. Adapted from Kim *et al.*

Figure 2.8 Energy band diagrams of a MoS_2 FET device (a) prior to proton irradiation (no irradiation) and (b) after proton irradiation with high beam fluence (10^{13} and 10^{14} cm^{-2}). E_F: Fermi level energy, E_C: conduction band minimum, E_V: valence band maximum, Φ_B: Schottky barrier height. The green arrow indicates the proton beam irradiation, the blue circles with plus signs represent the oxide trapped charges, and the red circles with minus signs represent the interface trapped charges. Adapted from Kim *et al.*

Figure 3.1 Mechanical exfoliation of atomically thin MoS_2 flake by scotch tape.

Figure 3.2 (a) MoS_2 synthesis process. (b) PL peak-position mapping of CVD-grown MoS_2 film. (c) Statistical analysis of PL peak-position in CVD-grown MoS_2 triangular island and film. Adapted from Kim *et al.*

Figure 3.3 (a) Optical micrograph of CVD-grown monolayer MoS_2 (left area) and a no-growth SiO_2 (right area) substrate. (b) AFM image of CVD-grown monolayer MoS_2 triangular islands (the profile indicates the thickness of triangular islands along the blue line). (c) Raman spectra of three different MoS_2 samples. (d) PL spectra of three different points of CVD-grown films. The inset image shows linear scale PL image of triangular islands. Adapted from Kim *et al.*

Figure 3.4 (a) Optical image showing a CVD-grown monolayer MoS_2 FET. The inset shows the schematics of the device. (b) Raman and PL spectra of a CVD-grown monolayer MoS_2. (c, d) Representative electrical characteristics of the CVD-grown monolayer MoS_2 FET. (c) I_{DS}–V_{DS} curves measured for different gate voltages at room temperature. (d) I_{DS}–V_{GS} curves measured at a fixed V_{DS} = 0.5 V for various temperatures. Adapted from Kim *et al.*

Figure 4.1 (a) Schematic illustrations and a representative optical image (in grey background) of the fabrication of CVD-grown monolayer MoS_2 FETs with inkjet-printed Ag electrodes. (b) Representative optical images of sessile drops on CVD-grown monolayer MoS_2 film. The top and bottom images show the Ag ink and DI water drops on the MoS_2 film, respectively. (c) The surface profiles of CVD-grown monolayer MoS_2 films with inkjet-printed Ag electrodes. Adapted from Kim *et al*,.

Figure 4.2 Representative electrical characteristics of the CVD-grown monolayer MoS_2 FET with the inkjet-printed Ag electrodes. (a) Transfer characteristics (I_{DS}–V_{GS}) measured at different V_{DS}. The inset figure shows the same transfer characteristics on a log scale. (b) Output characteristics (I_{DS}–V_{DS}) measured at different V_{GS}. (c) Log-Log plot of output characteristics in low V_{DS} region. The red dashed lines indicate the fitting line to the $I_{DS} \propto V_{DS}^{\gamma}$ relationship. Adapted from Kim *et al*,.

Figure 4.3 (a) $1/\sqrt{g_m}$ and Y-function ($I_{DS}/\sqrt{g_m}$)of the CVD-grown monolayer MoS_2 FET with inkjet-printed electrodes at V_{DS} of 1 V. (b) Graph of the total resistance (R_{tot}) *versus* V_{GS} graph at V_{DS} of 20 V; the enlarged image shows the R_{tot} at V_{GS} from 5 to 20 V. The red dashed line shows the slope around V_{DS} of 15 V. Adapted from Kim *et al*,.

Figure 4.4 Transfer characteristics measured in ambient with respect to the different gate-bias stress time up to 10,000 sec on (a) log and (b) linear scales. The gate-bias stress voltage V_{GS} was 30 V. The inset of (b) shows the change of normalized subthreshold swing (S.S.) with respect to the stress time. (c) Threshold voltage shift (ΔV_{th}) with respect to the value of pre-stress curve. The solid red line represents a stretched-exponential fitting to the experimental data using equation (7). The inset figure shows the ΔV_{th} on a log scale. Adapted from Kim *et al*,.

Figure 5.1 (a) Cleaned the SiO_2/Si substrate. (b) CVD-grown MoS_2 on the SiO_2/Si substrate. (c) MoS_2 patterning process using RIE while covered with a shadow mask. (d) Clearly patterned monolayer MoS_2 film. (e) Spin-coated the PMMA supporting layer onto MoS_2/SiO_2. (f) After detaching the monolayer MoS_2 film from SiO_2 using a KOH solution, the MoS_2/PMMA structure was placed on the PEN substrate. (g) Transferred the MoS_2 onto the PEN substrate. Direct inkjet-printing of (h-i) PEDOT:PSS *S/D* electrodes, (j) PVP dielectric layer and (k) PEDOT:PSS gate electrodes. Adapted from Kim *et al.*

Figure 5.2 (a) Transmittance spectra of the layer-by-layer stacked device structures from the bare PEN substrate to fully stacked structures (PEDOT:PSS/PVP/PEDOT:PSS/MoS_2/PEN films). (b) Schematic of the stacked structures. Adapted from Kim *et al.*

Figure 5.3 (a) Schematic illustration of the fabrication processes for fully printed, flexible and transparent CVD-synthesized MoS_2 phototransistors. (b) Contact angle

measurements of PEDOT:PSS (top) and PVP (bottom) ink on the MoS_2 film (left) and PEN substrate (right). (c) Digital images of the transparent MoS_2 phototransistor arrays. In the left image, the device arrays (marked with a red square) were placed on a piece of paper with university symbols. The right image was taken in front of a building. (d) Photographic image (inset) and schematic of the devices under laser illumination. Adapted from Kim *et al.*

Figure 5.4 (a) Raman spectrum of a CVD-synthesized monolayer MoS_2 film on a SiO_2/Si substrate. (b) PL spectra of CVD-synthesized monolayer MoS_2 films on SiO_2/Si and PEN substrates. The inset shows a PL intensity mapping at 670 nm (= 1.85 eV). Scale bar is 5 μm. (c) EDS data of Mo (blue line) and S (yellow line) and a cross-sectional STEM image of a CVD-synthesized MoS_2 film on a SiO_2/Si substrate. Scale bar is 5 nm. (d) Optical images of a CVD-synthesized MoS_2 channel before (top) and after (bottom) selective patterning processes. Scale bar is 400 μm. (e) XPS spectra of a CVD-synthesized monolayer MoS_2 film on a SiO_2/Si (top) substrate and transferred MoS_2 film on the PEN (bottom) substrate. (f) Transmittance spectra of a bare PEN substrate (blue line) and fully stacked films (red line). Adapted from Kim *et al*.

Figure 5.5 (a) I_{DS}–V_{GS} curves using a log scale at V_{DS} = 1 V. Inset represents the I_{DS}–V_{GS} curves using a linear scale. The change in mobility (μ) and subthreshold swing (*SS*) versus (b) number of bending cycles with a bending radius = 5 mm and (c) bending radii of 5, 7.5, 11, 15 and ∞. Adapted from Kim *et al.*

Figure 5.6 (a) The ratio of I_{light} (= I_{ph} + I_{dark}) to I_{dark} in the ON and OFF states as a function of a) wavelength and (b) laser power at a fixed V_{DS} = 10 V. Insets of (a) and (b) exhibit I_{ph} versus V_{GS} and the change in V_{th} with respect to the laser power, respectively. As the laser power increased, V_{th} shifted in the negative voltage direction, which indicates an increase in I_{ph} in the subthreshold regime. (c) Time-resolved photocurrent measurement under laser illumination (λ = 520 nm). The green-shaded regions indicate laser illumination for 20 s. (d) Responsivity of phototransistors as a function of power density under laser illumination (λ = 520 nm). (e) Photoresponsivity, photodetectivity and (f) external quantum efficiency as a function of wavelength at a fixed V_{GS} = 80 V, V_{DS} = 10 V and laser power density = 57.3 W/m^2. Adapted from Kim *et al.*

1. Introduction

1.1. Graphene and 2D materials

Graphene has been highly favored due to its fascinating properties such as high mechanical strength, small thickness, and flexibility, etc. Most of all, due to its extremely high electrical mobility, graphene has been studied for next-generation electronic components [1–3]. However, graphene has a critical shortcoming to be used as a channel layer, because it does not have band gap energy intrinsically. So, in order to overcome this, researchers tried to dope graphene chemically or fabricated nano-ribbon shape graphene to open a band gap artificially [4]. Though the band gap can be induced in specially-treated graphene, electrical properties like mobility are reduced to be fully utilized as an electronic device.

1.2. Molybdenum disulfide (MoS_2)

After knowing the interesting features of 2-dimensional (2D) materials by graphene, researchers tried to find another 2D materials which can be used in electronics. In this sense, transition metal dichalcogenides (TMDCs) which are composed of three atoms– one from transition metals, and the other two from the oxygen-group elements (chalcogen)– have been studied [5]. These TMDC materials have a covalent bonding in-plane direction, and weak Van der Waals bonding in out-of-plane direction. So, it can be easily exfoliated using sticky tape. Among many TMDCs, molybdenum disulfide (MoS_2) channel field-effect transistors (FETs) have been studied widely. MoS_2 FETs have many good characteristics such as high mobility, On/Off ratio, thin layer and tunable band gap energy according to its thickness [6].

References

1. Geim, A. K.; Novoselov, K. S. The rise of graphene. *Nat. Mater*. **2007**, *6*, 183–191.
2. Novoselov, A. K.; Fal'ko, V. I.; Colombo, L.; Gellert, P. R.; Schwab, M. G.; Kim, K. A roadmap for graphene. *Nature* **2012**, *490*, 192–200.
3. Allen, M. J.; Tung, V. C., Kaner, R. B. Honeycomb Carbon: A Review of Graphene. *Chem. Rev*. **2010**, *110*, 132–145.
4. Han, M. Y.; Özyilmaz, B.; Zhang, Y.; Kim, P. Energy Band-gap Engineering of Graphene Nanoribbons. *Phys. Rev. Lett*. **2007**, *98*, 206805.
5. Chhowalla, M.; Shin, H. S.; Eda, G.; Li, L.-J.; Loh, K. P.; Zhang, H. The chemistry of two-dimensional layered transition metal dichalcogenide nanosheets. *Nat. Chem*. **2013**, *5*, 263–275.
6. Radisavljevic, B.; Radenovic, A.; Brivio, J.; Giacometti, V.; Kis, A. Single-Layer MoS_2 Transistors. *Nat. Nanotechnol.* **2011,** *6*, 147-150.

2. Proton beam irradiation effect on atomically thin MoS_2 field-effect transistors

2.1. Introduction

Recently, two-dimensional (2D) transition-metal dichalcogenide (TMD) materials have gained significant attention due to their potential applications in atomic-film devices [1–4]. Graphene, one of the most popular of these 2D materials, has been widely studied but has limited utility as a semiconductor because it lacks an energy band gap [5]. Unlike graphene, TMD materials such as MoS_2, $MoSe_2$, and WSe_2, possess a band gap and semiconducting properties [6–8]. In particular, molybdenum disulfide (MoS_2) has an indirect band gap of 1.2 eV as a bulk material and a direct band gap of 1.8 eV as a single layer [4, 8]. Numerous studies have explored the application of 2D TMD materials in nanoelectronic devices because of their semiconducting properties [9–14]. For example, researchers have demonstrated that MoS_2-based field effect transistor (FET) devices have outstanding electrical characteristics; single-layer MoS_2 device exhibits a high mobility (~200 cm^2/Vs) with near-ideal subthreshold swing down to 74 mV/decade and a high on/off ratio (~10^8) [15].

The ability to tailor the electrical properties of MoS_2 FETs would provide numerous advantages. In particular, to prepare a logic circuit using MoS_2, it is necessary to control the operation voltage. When trap states are introduced at the MoS_2 active layer and dielectric layer, the electrical properties of the device, such as the current and threshold voltage, are affected by charge trapping to these trap states. Attempts to tailor the electrical properties of FET devices made with carbon nanotubes [16, 17] or semiconducting nanowires [18, 20] have been made using irradiation with high energy particles. Originally, high energy particle beams of protons, electrons, or ions were used to impact silicon-based metal-oxide-semiconductor (MOS) devices in order to modify the electrical properties of the devices or investigate the properties under outer space conditions [21–24].

A few theoretical and experimental studies have investigated the irradiation of MoS_2 materials with electrons, protons, or heavy ions. Komsa *et al.* studied the

effects of electron beam irradiation on 2D TMD materials using first-principle simulations and experimental studies of single-layer MoS_2 devices irradiated by electron beams in a transmission electron microscope (TEM) operating at 20 keV [25]. Ochedowski *et al.* demonstrated the deterioration of MoS_2 FETs following 1.14 GeV U^{28+} ion beam irradiation [26]. And, Mathew *et al*. studied ferromagnetism in MoS_2 bulk materials following 2 MeV proton beam irradiation [27]. However, a comprehensive study of high energy particle beams on MoS_2 atomic film-based FET devices have not yet been investigated. Therefore, it would be important to understand and develop irradiation-mediated engineering in MoS_2 FET devices.

Here, we studied the effect of proton irradiation on MoS_2 FET devices prepared with a few layers of MoS_2 flakes. The devices were irradiated with 10 MeV proton beams under fluence conditions of 10^{12}, 10^{13}, and 10^{14} cm^{-2}, corresponding to beam irradiation times of 20, 200, and 2000 seconds, respectively. We systematically measured and compared the electrical properties of the devices, including current level, conductance, and threshold voltage, before and after proton irradiation for each proton beam fluence condition. The changes in the electrical properties of the proton-irradiated devices can be attributed to irradiation-induced traps, such as positive oxide-charge traps in the SiO_2 layer and interface trap states.

2.2. Experiments

2.2.1. Device fabrication process

The multi-layer MoS_2 flakes were transferred by 3M Scotch tape to SiO_2 on a heavily doped p++ Si wafer (resistivity ~5×10^{-3} Ω·cm) that can be used as a back gate. The MoS_2 flakes were transferred onto silicon substrate by the mechanical exfoliation using a scotch tape from a bulk MoS_2 crystal (purchased from SPI Supplies). The location of a MoS_2 flake was found using an optical microscope, then the MoS_2 flake's height was measured with a NX 10 AFM system (Park Systems). In order to make patterns of electrodes, we spin-coated MMA (8.5) MAA (9% concentration in ethyl lactate) and PMMA 950K (5% concentration in anisole) at 4000 rpm for 50 sec. After the two-step spin-coating, the sample was baked at 180 °C for 90 s on a hot plate. The electrodes were patterned using an electron beam

lithography system (JSM-6510, JEOL) with a 30 kV exposure. For the development of pattern, MIBK:IPA (1:3) solution was used with a development time of 50 s.

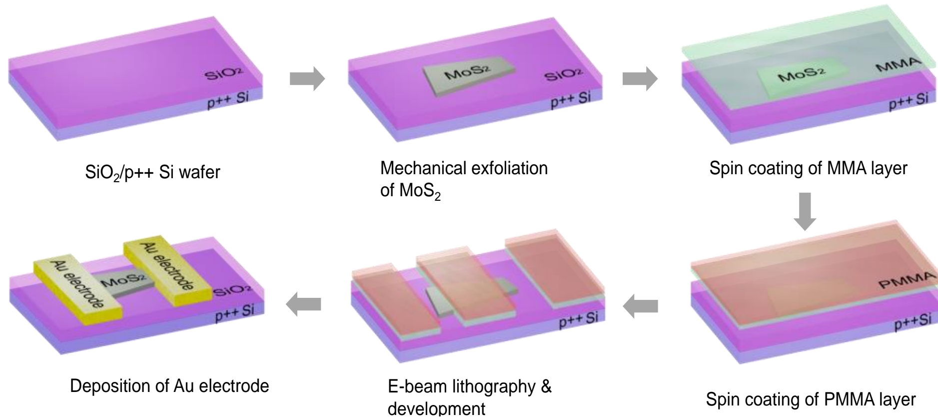

Figure 2.1 Schematic illustration of device fabrication process. Adapted from Kim *et al.* [43]

The Raman spectroscopic measurements were done with a Raman spectrometer (T64000 Horiba Jobin Yvon, at National Center for Inter-University Research Facilities) that uses an Ar ion laser (wave length of 514.5 nm) as a source.

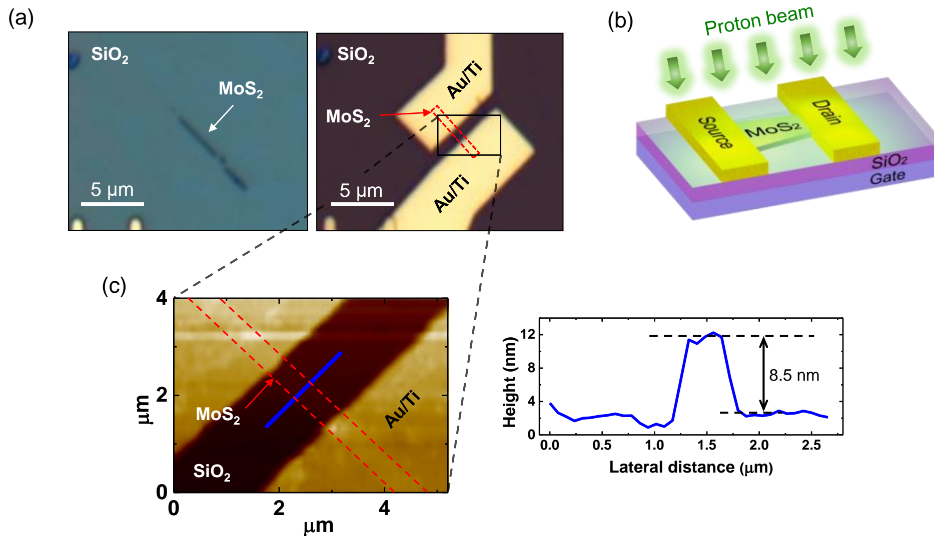

Figure 2.2 (a) Optical images showing the fabrication of a MoS_2 FET device. (b) Schematic illustration of proton beam irradiation on a MoS_2 FET device. (c) AFM image of the MoS_2 FET device with a cross-sectional topographic profile indicated by the blue line (MoS_2 flake). Red dashed-lines in (a) and (c) indicate MoS_2 flakes. Adapted from Kim *et al.* [43]

2.2.2. Proton beam irradiation experiment

The proton beam facility used for this research was the MC-50 cyclotron at the Korea Institute of Radiological and Medical Sciences. The proton beam exhibited an energy of 10 MeV, an average beam current of 10 nA, and a beam uniformity of approximately 90%. Beam irradiation time of 20, 200, and 2000 seconds were investigated, corresponding to total fluence (or dose) values, Φ, of ~10^{12}, 10^{13}, and 10^{14} cm^{-2}.

2.2.3. Electrical characteristics measurements

All the electrical measurements were conducted with a probe station (JANIS, ST-500) using a semiconductor parameter analyzer (HP 4145B) at room temperature in a vacuum (~10^{-4} torr). The fabricated MoS_2 FET devices were divided into three groups according to the proton beam fluence conditions. The electrical characteristics of each device were measured before and after proton irradiation and systematically compared.

2.3. Results and discussions

2.3.1. Electrical characteristics

Fig. 2.3 illustrates the electrical characteristics of the MoS_2 FET devices. The left and right plots in Fig. 2.3 (a) show the output characteristics (source-drain current *versus* source-drain voltage, I_{DS}–V_{DS}) measured for a MoS_2 FET at gate voltages (V_{GS}) ranging from -30 to 30 V in increments of 10 V before and after, respectively, proton beam irradiation with a fluence of 10^{12} cm^{-2} (corresponding to an irradiation time of 20 sec). Fig 2.3 (b) shows the transfer characteristics (source-drain current *versus* gate voltage, I_{DS}–V_{GS}) of the same device at a fixed source-drain voltage (V_{DS}) of 0.5 V before and after proton irradiation under the same proton beam conditions used in Fig 2.3 (a). The MoS_2 FET device exhibited n-channel behavior, with the current increasing as a more positive gate voltage was applied. The results in Fig 2.3 (a) suggest that the electrical properties of the MoS_2 FET device did not change substantially following the proton irradiation with a small fluence condition of 10^{12} cm^{-2} (*i.e.,* a short proton irradiation time of 20 sec). However, the MoS_2 FET

devices were influenced noticeably when irradiated with the proton beam for a longer period of time. Fig. 2.3 (c) shows the output characteristics measured for another MoS_2 FET device before and after proton beam irradiation with a fluence of 10^{14} cm^{-2} (corresponding to an irradiation time of 2000 sec). Fig. 2.3 (d) displays the corresponding transfer characteristics. Importantly, we observed that the current of the device decreased dramatically following proton beam irradiation. For example, the current of the device was measured as ~20 μA at V_{DS} = 5 V and V_{GS} = 20 V prior to proton irradiation, whereas after proton irradiation, the current was measured as ~1 μA under the same measurement conditions (see inset of the plot on the right in Fig. 2.3 (c)). Hence, the current decreased by nearly 95% as a result of proton irradiation. This effect was clearly observed in the transfer curves (Fig. 2.3 (d)); *i.e.*, the current decreased significantly following proton beam irradiation.

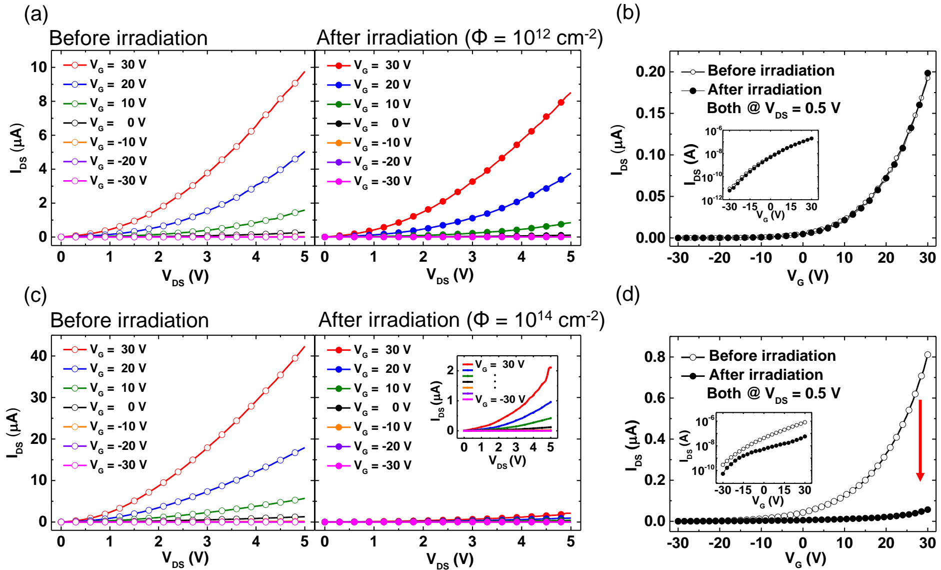

Figure 2.3 Representative electrical characteristics of MoS_2 FET devices. (a) Before and (b) after proton irradiation with a beam fluence of 10^{12} cm^{-2}. (c) Before and (d) after proton irradiation with a fluence of 10^{14} cm^{-2}. (a, c) Output characteristics (I_{DS}–V_{DS}) measured for different gate voltages. (b, d) Transfer characteristics (I_{DS}–V_{GS}) measured at a fixed V_{DS} = 0.5 V. The inset figures of (b) and (d) are the transfer characteristics on a log scale. Adapted from Kim *et al.* [43]

For the MoS_2 FET devices irradiated by a proton beam with a fluence of 10^{13} cm^{-2} (corresponding to an irradiation time of 200 sec), the current level also decreased following proton irradiation, although the decrease was smaller than that observed under a fluence of 10^{14} cm^{-2}; the current decreased from ~17.5 μA (before proton irradiation) to ~5 μA (after proton irradiation) when measured at V_{DS} = 5 V and V_{GS} = 20 V, as shown in **Fig. 2.4.**

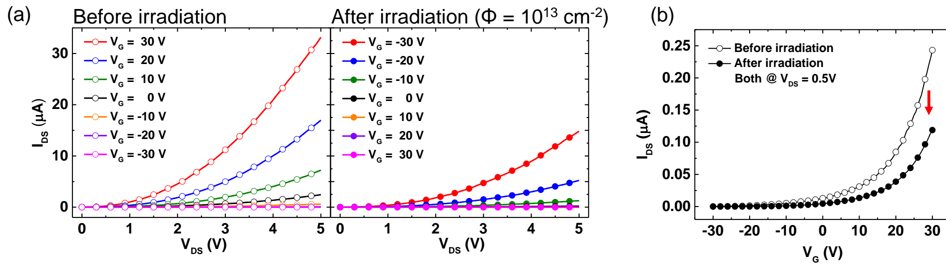

Figure 2.4 Representative electrical characteristics of a MoS_2 FET device before and after proton irradiation with a beam fluence of 10^{13} cm^{-2} (corresponding to an irradiation time of 200 sec). (a) I_{DS}–V_{DS} curves measured for different gate voltages before (left) and after (right) proton irradiation. (b) I_{DS}–V_{GS} curves measured at a fixed V_{DS} = 0.5 V before (open circles) and after (filled circles) proton irradiation. Adapted from Kim *et al.* [43]

The subthreshold slope of the device that was irradiated with low-fluence proton beam (10^{12} cm^{-2}) was almost the same before and after the proton irradiation, as shown in the inset of Fig. 2.3 (b). On the contrary, the subthreshold slope of the device that was irradiated with high-fluence proton beam (10^{14} cm^{-2}) became worse after the proton irradiation, as shown in the inset of Fig. 2.3 (d). Such degradation of the subthreshold slope after high-fluence proton beam irradiation is attributed to the proton beam-induced trap states at the interface.

2.3.2. Dose-dependence and Raman spectra

Figs. 2.5 (a)–(c) show the statistical results for the MoS_2 FET devices that were irradiated by proton beams under the three different fluence conditions. Here, we measured three devices under each fluence condition. A total of nine MoS_2 FET devices were therefore investigated, divided into three groups, and exposed to proton beams under the three different beam fluence conditions of 10^{12}, 10^{13}, and 10^{14} cm^{-2}. We subsequently compared the measurements before and after each proton irradiation condition. The error bars in the figures represents the standard deviations from the individual measurements. In Fig. 2.5 (a), the current levels of the proton-irradiated devices measured at $V_G = 30$ V and $V_{DS} = 0.5$ V were compared with those of the devices before proton irradiation. The normalized current value in Fig. 2.5 (a) means the ratio of the current of the proton-irradiated device to that (value = 1.0, dashed line) of the same device before-proton-irradiation case. In Fig. 2.5 (b), the normalized conductance values were calculated and compared in a similar manner as in Fig. 2.5 (a). Here, the low-field conductance values were determined from the slope for a linear segment at the low bias region ($-0.3 < V_{DS} < 0.3$ V). Fig. 2.5 (c) displays the changes in threshold voltages following proton irradiation. First, the current, conductance, and threshold voltage values for the devices irradiated by proton beams under a low fluence of 10^{12} cm^{-2} did not change significantly. In the contrast, for the devices irradiated by a proton beam with a medium fluence of 10^{13} cm^{-2}, the current and conductance values decreased substantially, accompanied with a shift of the threshold voltage to the positive gate voltage direction. These changes in the current, conductance, and threshold voltage became more significant for the devices irradiated by proton beams with a high fluence of 10^{14} cm^{-2}, as indicated by the greater decreases in the current and conductance and the more positive shifts of the threshold voltage.

We measured Raman spectra of MoS_2 flakes before and after proton beam irradiation with the fluences of $\Phi = 10^{12}$ cm^{-2} (Figure 3(d)) and $\Phi = 10^{14}$ cm^{-2} (Fig. 2.5 (e)). The two prominent E^1_{2g} (~380 cm^{-1}) and A_{1g} (~405 cm^{-1}) peaks are due to in-plane and out-of-plane vibrations of MoS_2 atoms [28], as illustrated in Fig. 2.5 (f). There was no significant change found in the E^1_{2g} and A_{1g} modes of MoS_2 in the Raman spectra before and after the proton irradiation. Note that we did Raman or

electrical measurements on the proton-irradiated samples at least 1 day after the proton irradiation because we were not allowed to pick up the proton-exposed samples right after the proton irradiation due to the radioactivity safety regulation. Importantly, we observed significant changes in the electrical properties of MoS_2 FETs (Figs. 2.3 and 2.5 (a)–(c)) while we didn't observe noticeable changes in the Raman spectra of MoS_2 flakes (Figs. 2.3 and 2.5 (d)–(e)). These results suggest that the change of the electrical characteristics of MoS_2 FET devices after the proton irradiation is not due to MoS_2 itself, instead it is due to the proton-irradiation-induced oxide traps in the SiO_2 layer or the interface trap states at the SiO_2/MoS_2 interface.

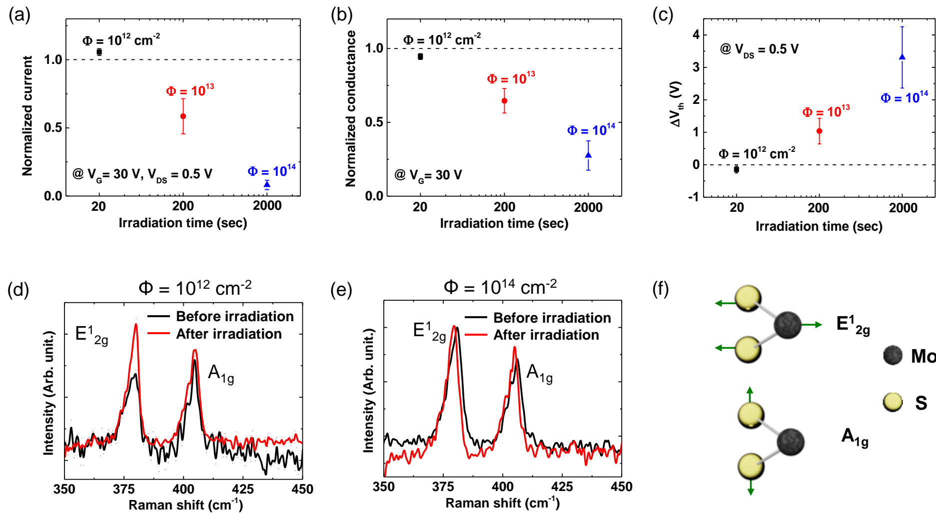

Figure 2.5 Statistical data for the (a) normalized conductance, (b) normalized current, and (c) change in the threshold voltage of the devices following proton irradiation with different beam fluences (10^{12}, 10^{13}, and 10^{14} cm^{-2}). Raman spectra of MoS_2 flakes before and after proton beam irradiation with the fluences of (d) $\Phi = 10^{12}$ cm^{-2} and (e) $\Phi = 10^{14}$ cm^{-2}. (f) Schematic illustrations of MoS_2 vibration modes. Adapted from Kim *et al.* [43]

2.3.3. Time-dependence

We investigated the time-dependence of the electrical characteristics of the proton-irradiated devices by measuring the devices before proton irradiation and 1 day, 3 days, and 5 days after proton irradiation. **Figs. 2.6** (a)–(c) show the transfer curves of three MoS_2 FET devices that were irradiated by proton beams with fluence conditions of either 10^{12}, 10^{13}, or 10^{14} cm^{-2}. For the 10^{12} cm^{-2} fluence condition, the current of the proton-irradiated device remained nearly constant with time (Figure 4(a)), consistent with the results of Figs. 2.3 and 2.4. For the cases of the 10^{13} and 10^{14} cm^{-2} fluences, the currents of the proton-irradiated devices decreased following proton irradiation (for example, see the day 1 data). However, the current typically recovered; for the middle fluence condition (10^{13} cm^{-2}), the current recovered to nearly its original level after 5 days (Fig 2.6 (b)), whereas for the high fluence condition (10^{14} cm^{-2}), the current recovered but remained diminished even after 5 days (Fig. 2.6 (c)). Figs. 2.6 (d)–(f) summarize the normalized current, normalized conductance, and changes in the threshold voltage before and after proton irradiation with fluence conditions of 10^{12}, 10^{13}, and 10^{14} cm^{-2}. These plots show that the electrical parameters were not significantly influenced by the weak fluence proton irradiation (10^{12} cm^{-2}) and that these values typically recovered with time but that the recovery was not complete for the high fluence proton irradiation (10^{14} cm^{-2}).

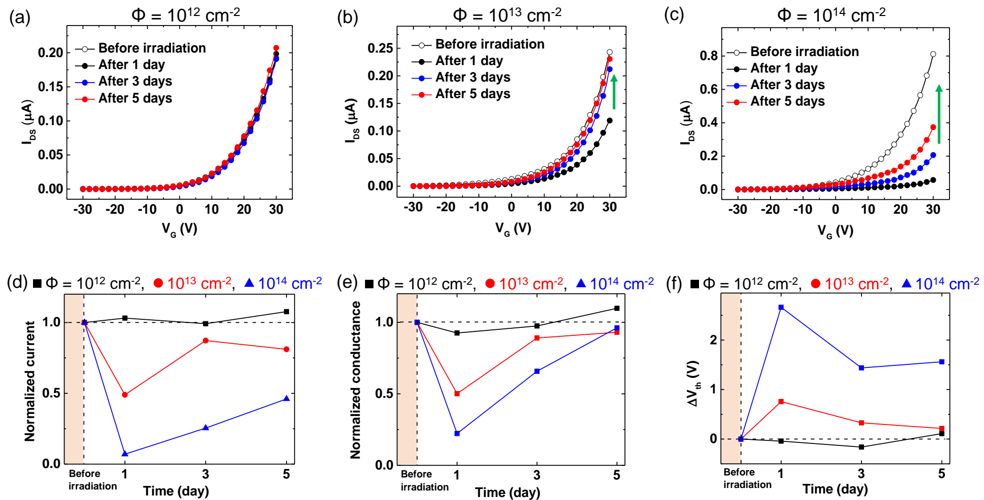

Figure 2.6 Time-dependence of the I_{DS}–V_{GS} curves of the MoS_2 FET devices before proton irradiation and 1, 3, and 5 days after proton irradiation with fluences of (a)

10^{12} cm^{-2}, (b) 10^{13} cm^{-2}, and (c) 10^{14} cm^{-2}. The (d) normalized current, (e) normalized conductance and (f) change in the threshold voltages of the devices are plotted as a function of time (i.e., before proton irradiation and at 1, 3, and 5 days after proton irradiation) for the three different fluence conditions of 10^{12}, 10^{13}, and 10^{14} cm^{-2}. Adapted from Kim *et al.* [43]

2.3.4. Stopping and Range of Ions in Matter (SRIM)

When high energy particles are irradiated on silicon-based materials and devices, they lose the majority of their energy near the stopping position [29,30]. We calculated the energy-loss depth profiles of irradiated protons using Stopping and Range of Ions in Matter (SRIM 2008) software, which is a computer program that calculates the interactions of energetic particles with matter. The SRIM simulation results are provided in **Fig. 2.7** [30,31]. From these simulation results, we found that protons could penetrate and stop ~700 μm from the top surface. Because the structure of our MoS_2 FET devices comprised stacks of $MoS_2/SiO_2/Si$ (2–8 nm/270 nm/500 μm), the majority of protons could simply penetrate through the entire structure, generating electron-hole pairs along the path of the proton beam.

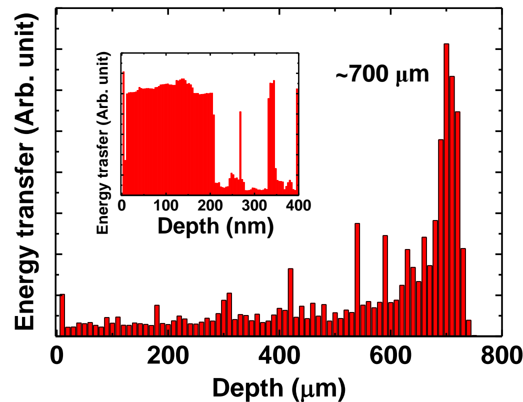

Figure 2.7 Energy loss depth profiles of irradiated protons calculated using SRIM. The inset image is a zoomed plot for the energy loss depth profile in the range of 0–400 nm from the top surface. Adapted from Kim *et al.* [43]

It is known that when high energy particles such as electrons and protons are irradiated on silicon-based FET devices, they can ionize atoms and generate electron-hole pairs in the oxide (SiO_2) layer which is the layer that is most sensitive to ionizing irradiation [32,33]. The generated electrons are quickly swept out of the bulk SiO_2 layer in a few picoseconds due to their high mobility [34]. The remaining holes wander through the SiO_2 layer and may be trapped at localized trap sites in the bulk SiO_2 layer, leading to positive oxide-trapped charges. In addition, the irradiation-induced holes and protons in the SiO_2 can transport to the SiO_2/MoS_2 interface, leading to the formation of interface trap states, which are negatively charged electron trap centers for n-channel transistors. The positive oxide traps in the SiO_2 layer enhance the gate electric field, leading to an increased carrier concentration. In contrast, the negative interface trap states act as electron trap centers, leading to a reduction in the carrier concentration. Furthermore, the irradiation-induced interface trap states occur on a time scale that is much slower than that of the positive oxide-charge traps in the SiO_2 layer. Therefore, the effects of proton irradiation on the MoS_2 FET devices can be attributed to the combined effects of positive oxide-charge traps in the SiO_2 layer and interface trap states [35,37].

For low fluence (short irradiation time) proton irradiation, neither positive oxide-charge traps nor interface trap states will be generated in sufficient quantities to significantly affect the electrical characteristics of the devices. As a result, no significant changes in the electrical parameters of the proton-irradiated devices were observed for proton irradiation under a 10^{12} cm^{-2} fluence (see Figs. 2.3 (a), 2.3 (b), 2.5 (a)–(c), 2.6 (a), and 2.6 (d)–(f)). However, at high fluence (long irradiation time), the interface trap states will play a major role in influencing the electrical performances of the proton-irradiated devices. These effects were observed in the MoS_2 FET devices irradiated by proton beams with 10^{13} or 10^{14} cm^{-2} fluences (Figs. 2.3 (c), (d), 2.5 (a)–(c), and 2.6 (b)–(f)). Note that for the 10^{12} cm^{-2} fluence condition, the currents of a portion of the proton-irradiated devices increased slightly compared with those measured prior to proton irradiation (see Fig. 2.5 (a)), which could be due to the effect of positive oxide-trap charges in the SiO_2 layer. However, this effect was too small to be confirmed, and a modified experimental design would be necessary to distinguish the effect of the positive oxide-trap charges in the SiO_2 layer

from that of the interface trap states. The recovery phenomena (Fig. 2.6) can also be attributed to the traps generated by the proton irradiation [37,38]. The recovery of the current indicates that the proton-irradiation-induced traps are not permanent and do not act as charge traps for an extended period unless the fluence of the proton irradiation is beyond a certain threshold. We observed that the current was fully recovered for a middle fluence of 10^{13} cm^{-2} approximately 5 days after proton irradiation (Fig. 2.6 (b)), but was not fully recovered at this time point for the high fluence condition of 10^{14} cm^{-2} (Fig. 2.6 (c)).

2.3.5. Energy band diagram

The observations in this study can be explained using energy band diagrams, as shown in **Fig. 2.8**. Fig. 2.8 (a) shows the energy band diagrams for V_{DS} = 0 V and V_{GS} = 0 V. The MoS_2 flakes have a band gap of ~1.2 eV, which is similar to the band gap of bulk MoS_2 [8]. In addition, the work function (Φ_{MoS2}) and electron affinity (χ_{MoS2}) of the flakes are 4.6–4.9 eV and ~4.0 eV, respectively [39-42]. We used Au/Ti as the source and drain electrodes in contact with the MoS_2 and a work function for Au (Φ_{Au}) of 5.4 eV and that for Ti (Φ_{Ti}) of 4.3 eV [41]. Therefore, the contact between Ti and MoS_2 will have a very small Schottky barrier (Φ_B), as indicated in the energy band diagram (Fig. 2.8 (a), right) [41]. When protons are irradiated on the devices, the proton beam induces positive oxide-trap charges in the SiO_2 layer and interface trap states at the SiO_2/MoS_2 interface. When the proton beam fluence is sufficient, the interface trap states influence the current flow in the MoS_2 channel, which hinders charge flows by trapping conduction electrons in the n-channel MoS_2. This will decrease the conduction electron concentration, raising the conduction band. In other words, an increasing interface trap density in the channel region by proton irradiation increases trapped electrons in the channel and reduces the current conductance, as shown in the right panel in Fig. 2.8 (b).

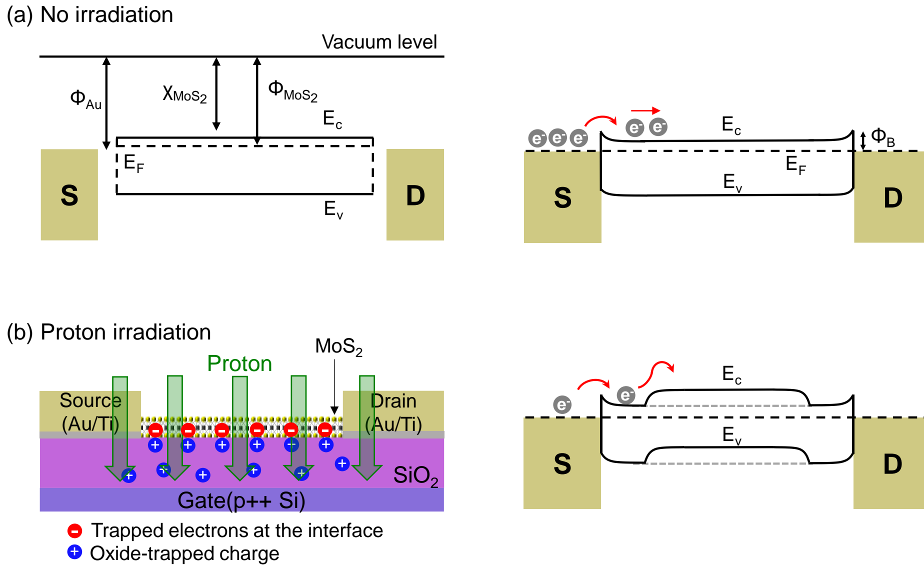

Figure 2.8 Energy band diagrams of a MoS_2 FET device (a) prior to proton irradiation (no irradiation) and (b) after proton irradiation with high beam fluence (10^{13} and 10^{14} cm^{-2}). E_F: Fermi level energy, E_C: conduction band minimum, E_V: valence band maximum, Φ_B: Schottky barrier height. The green arrow indicates the proton beam irradiation, the blue circles with plus signs represent the oxide trapped charges, and the red circles with minus signs represent the interface trapped charges. Adapted from Kim *et al.* [43]

2.4. Conclusion

In summary, we studied the effect of proton beam irradiation on multi-layer MoS_2 FET devices. The n-channel MoS_2 FET devices irradiated by proton beams with sufficiently high fluence conditions exhibited decreases in the current and conductance and a shift of the threshold voltage toward positive gate voltage direction. The recovery of these changes was observed over a time scale of days. These phenomena can be attributed to the interface trap states at the SiO_2/MoS_2 interfaces. This study improves our understanding of the influence of high energy proton beams on MoS_2-based nanoelectronic devices and may provide a method to control the electrical properties of MoS_2 FET devices through changing interface states using proton beams.

References

1. Chhowalla, M.; Shin, H. S.; Eda, G.; Li, L.-J.; Loh, K. P.; Zhang, H. The Chemistry of Two-Dimensional Layered Transition Metal Dichalcogenide Nanosheets. *Nat. Chem.* **2013**, *5*, 263–275.
2. Wang, Q. H.; Kalantar-Zadeh, K.; Kis, A.; Coleman, J. N.; Strano, M. S. Electronics and Optoelectronics of Two-Dimensional Transition Metal Dichalcogenides. *Nat. Nanotechnol.* **2012**, *7*, 699–712.
3. Fang, H.; Chuang, S.; Chang, T. C.; Takei, K.; Takahashi, T.; Javey, A. High-Performance Single Layered WSe_2 p-FETs with Chemically Doped Contacts. *Nano Lett.* **2012**, *12*, 3788–3792.
4. Mak, K. F.; Lee, C.; Hone, J.; Shan, J.; Heinz, T. F. Atomically Thin MoS_2: A New Direct-Gap Semiconductor. *Phys. Rev. Lett.* **2010**, *105*, 136805.
5. Schwierz, F. Graphene Transistors. *Nat. Nanotechnol.* **2010**, *5*, 487–496.
6. Jiang, H. Electronic Band Structures of Molybdenum and Tungsten Dichalcogenides by the GW Approach. *J. Phys. Chem. C* **2012**, *116*, 7664–7671.
7. Coehoorn, R.; Haas, C.; Dijkstra, J.; Flipse, C.; De Groot, R.; Wold, A. Electronic Structure of $MoSe_2$, MoS_2, and WSe_2. I. Band-Structure Calculations and Photoelectron Spectroscopy. *Phys. Rev. B* **1987**, *35*, 6195.
8. Kam, K.; Parkinson, B. Detailed Photocurrent Spectroscopy of the Semiconducting Group VI Transition Metal Dichalcogenides. *J. Phys. Chem.* **1982**, *86*, 463–467.
9. Yoon, J.; Park, W.; Bae, G. Y.; Kim, Y.; Jang, H. S.; Hyun, Y.; Lim, S. K.; Kahng, Y. H.; Hong, W. K.; Lee, B. H. Highly Flexible and Transparent Multilayer MoS_2 Transistors with Graphene Electrodes. *Small* **2013**, *9*, 3295–3300.
10. Sundaram, R. S.; Engel, M.; Lombardo, A.; Krupke, R.; Ferrari, A. C.; Avouris, P.; Steiner, M. Electroluminescence in Single Layer MoS_2. *Nano Lett.* **2013,** *13*, 1416-1421.
11. Radisavljevic, B.; Kis, A. Mobility Engineering and a Metal-Insulator Transition in Monolayer MoS_2. *Nat. Mater.* **2013,** *12*, 815–820.
12. Lopez-Sanchez, O.; Lembke, D.; Kayci, M.; Radenovic, A.; Kis, A. Ultrasensitive Photodetectors based on Monolayer MoS_2. *Nat. Nanotechnol.* **2013**, *8*, 497–501.
13. Lee, H. S.; Min, S.-W.; Chang, Y.-G.; Park, M. K.; Nam, T.; Kim, H.; Kim, J. H.; Ryu, S.; Im, S. MoS_2 Nanosheet Phototransistors with Thickness-Modulated Optical Energy Gap. *Nano Lett.* **2012,** *12*, 3695–3700.
14. Kim, S.; Konar, A.; Hwang, W.-S.; Lee, J. H.; Lee, J.; Yang, J.; Jung, C.; Kim, H.; Yoo, J.-B.; Choi, J.-Y. High-Mobility and Low-Power Thin-Film Transistors based on Multilayer MoS_2 Crystals. *Nat. Commun.* **2012,** *3*, 1011.

15. Radisavljevic, B.; Radenovic, A.; Brivio, J.; Giacometti, V.; Kis, A. Single-Layer MoS_2 Transistors. *Nat. Nanotechnol.* **2011,** *6*, 147–150.
16. Vijayaraghavan, A.; Kanzaki, K.; Suzuki, S.; Kobayashi, Y.; Inokawa, H.; Ono, Y.; Kar, S.; Ajayan, P. M. Metal-Semiconductor Transition in Single-Walled Carbon Nanotubes Induced by Low-Energy Electron Irradiation. *Nano Lett.* **2005,** *5*, 1575–1579.
17. Navarro, C.; De Pablo, P.; Gómez-Herrero, J.; Biel, B.; Garcia-Vidal, F.; Rubio, A.; Flores, F. Tuning the Conductance of Single-Walled Carbon Nanotubes by Ion Irradiation in the Anderson Localization Regime. *Nat. Mater.* **2005,** *4*, 534–539.
18. Gunho, J.; Hong, W.-K.; Choe, M.; Park, W.; Yung Ho, K.; Lee, T. Proton Irradiation-Induced Electrostatic Modulation in ZnO Nanowire Field-Effect Transistors with Bilayer Gate Dielectric. *IEEE Trans. Nanotechnol.* **2012,** *11*, 918–923.
19. Hong, W.-K.; Jo, G.; Sohn, J. I.; Park, W.; Choe, M.; Wang, G.; Kahng, Y. H.; Welland, M. E.; Lee, T. Tuning of the Electronic Characteristics of ZnO Nanowire Field Effect Transistors by Proton Irradiation. *ACS Nano* **2010,** *4*, 811–818.
20. Liao, L.; Lu, H.; Li, J.; Liu, C.; Fu, D.; Liu, Y. The Sensitivity of Gas Sensor based on Single ZnO Nanowire Modulated by Helium Ion Radiation. *Appl. Phys. Lett.* **2007,** *91*, 173110.
21. Childres, I.; Jauregui, L. A.; Foxe, M.; Tian, J.; Jalilian, R.; Jovanovic, I.; Chen, Y. P. Effect of Electron-Beam Irradiation on Graphene Field Effect Devices. *Appl. Phys. Lett.* **2010,** *97*, 173109.
22. Hu, X.; Karmarkar, A. P.; Jun, B.; Fleetwood, D. M.; Schrimpf, R. D.; Geil, R. D.; Weller, R. A.; White, B. D.; Bataiev, M.; Brillson, L. J. Proton-Irradiation Effects on AlGaN/AlN/GaN High Electron Mobility Transistors. *IEEE Trans. Nucl. Sci.* **2003,** *50*, 1791–1796.
23. Krasheninnikov, A.; Nordlund, K.; Sirviö, M.; Salonen, E.; Keinonen, J. Formation of Ion-Irradiation-Induced Atomic-Scale Defects on Walls of Carbon Nanotubes. *Phys. Rev. B* **2001,** *63*, 245405.
24. Srour, J. R.; McGarrity, J. M. Radiation Effects on Microelectronics in Space. *Proc. IEEE* **1988,** *76*, 1443–1469.
25. Komsa, H.-P.; Kotakoski, J.; Kurasch, S.; Lehtinen, O.; Kaiser, U.; Krasheninnikov, A. V. Two-Dimensional Transition Metal Dichalcogenides under Electron Irradiation: Defect Production and Doping. *Phys. Rev. Lett.* **2012,** *109*, 035503.
26. Ochedowski, O.; Marinov, K.; Wilbs, G.; Keller, G.; Scheuschner, N.; Severin, D.; Bender, M.; Maultzsch, J.; Tegude, F. J.; Schleberger, M. Radiation Hardness of Graphene and MoS_2 Field Effect Devices against Swift Heavy Ion Irradiation. *J. Appl.*

Phys. **2013,** *113*, 214306.

27. Mathew, S.; Gopinadhan, K.; Chan, T.; Yu, X.; Zhan, D.; Cao, L.; Rusydi, A.; Breese, M.; Dhar, S.; Shen, Z. Magnetism in MoS_2 Induced by Proton Irradiation. *Appl. Phys. Lett.* **2012,** *101*, 102103.
28. Lee, C.; Yan, H.; Brus, L. E.; Heinz, T. F.; Hone, J.; Ryu, S. Anomalous Lattice Vibrations of Single-and Few-Layer MoS_2. *ACS Nano* **2010**, 4, 2695–2700.
29. Messenger, S.; Burke, E.; Summers, G.; Xapsos, M.; Walters, R.; Jackson, E.; Weaver, B. Nonionizing Energy Loss (NIEL) for Heavy Ions. *IEEE Trans. Nucl. Sci.* **1999,** *46*, 1595–1602.
30. Ziegler, J. F.; Biersack, J. P. *The Stopping and Range of Ions in Matter*. Springer: 1985.
31. Ziegler, J. F.; Ziegler, M. D.; Biersack, J. P. SRIM-The Stopping and Range of Ions in Matter (2010). *Nucl. Instrum. Methods Phys. Res., Sect. B* **2010,** *268*, 1818–1823.
32. Schroder, D. K., *Semiconductor Material and Device Characterization*. John Wiley & Sons: 2006; Chapter 6.
33. Oldham, T. R., *Ionizing Radiation Effects in MOS Oxides*. World Scientific: 1999; Vol. 3.
34. Hughes, R. Chrage-Carrier Transport Phenomena in Amorphous SiO_2: Direct Measurement of the Drift Mobility and Lifetime. *Phys. Rev. Lett.* **1973,** *30*, 1333.
35. Sze, S. M.; Ng, K. K., *Physics of Semiconductor Devices*. 3rd ed.; Wiley-Interscience: 2007; Chapter 4.
36. Schwank, J. R.; Shaneyfelt, M. R.; Fleetwood, D. M.; Felix, J. A.; Dodd, P. E.; Paillet, P.; Ferlet-Cavrois, V. Radiation effects in MOS Oxides. *IEEE Trans. Nucl. Sci.* **2008,** *55*, 1833–1853.
37. Oldham, T. R.; McLean, F. Total Ionizing Dose Effects in MOS Oxides and Devices. *IEEE Trans. Nucl. Sci.* **2003,** *50*, 483–499.
38. McLean, F.; Boesch, H.; McGarrity, J. Hole Transport and Recovery Characteristics of SiO_2 Gate Insulators. *IEEE Trans. Nucl. Sci.* **1976,** *23*, 1506–1512.
39. Liu, K.-K.; Zhang, W.; Lee, Y.-H.; Lin, Y.-C.; Chang, M.-T.; Su, C.-Y.; Chang, C.-S.; Li, H.; Shi, Y.; Zhang, H. Growth of Large-Area and Highly Crystalline MoS_2 Thin Layers on Insulating Substrates. *Nano Lett.* **2012,** *12*, 1538–1544.
40. Giridharagopal, R.; Kelly, K. F. Substrate-Dependent Properties of Polydiacetylene Nanowires on Graphite and MoS_2. *ACS Nano* **2008,** *2*, 1571–1580.
41. Das, S.; Chen, H.-Y.; Penumatcha, A. V.; Appenzeller, J. High Performance Multilayer MoS_2 Transistors with Scandium Contacts. *Nano Lett.* **2013**, *13*, 100–105.
42. Han, S.; Kwon, H.; Kim, S. K.; Ryu, S.; Yun, W. S.; Kim, D.; Hwang, J.; Kang, J.-S.;

Baik, J.; Shin, H. Band-Gap Transition Induced by Interlayer Van Der Waals Interaction in MoS_2. *Phys. Rev. B* **2011,** *84*, 045409.

43. Kim, T.-Y.; Cho, K.; Park, W.; Park, J.; Song, Y.; Hong, S.; Hong, W.-K.; Lee, T. Irradiation effects of high energy proton beams on MoS_2 field effect transistors. *ACS Nano*, **2014**, *8*, 2774–2781.

3. Chemical vapor deposition of monolayer MoS_2 film

3.1. Introduction

3.1.1. Limit of mechanical exfoliation

Ultra-thin monolayer MoS_2 is one of the promising channel materials in optoelectronics devices, such as photosensors, photodetectors and photodiodes [1–8]. However, it is still difficult to produce large-area monolayer TMDC films, by widely used top-down methods, such as mechanical exfoliation [9], thinning [10], and liquid intercalation [11]. As we can see from the **Fig. 3.1** below, mechanically exfoliated MoS_2 samples are very small. Moreover, the number of layers cannot be controlled.

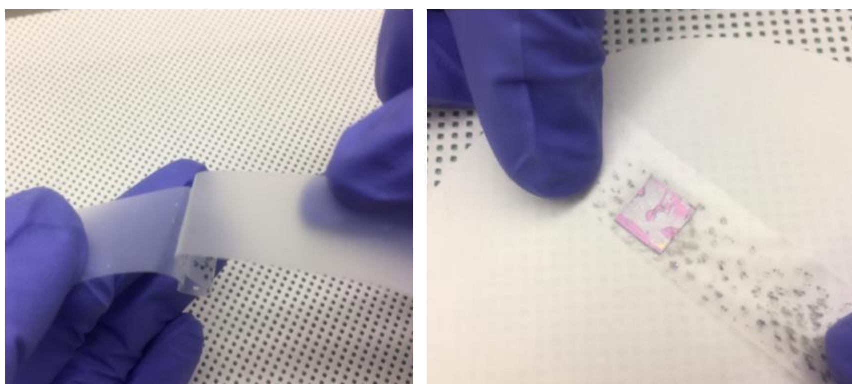

Figure 3.1 Mechanical exfoliation of atomically thin MoS_2 flake by sticky tape.

3.1.2. Many synthesis methods

In this regard, many bottom-up synthesis methods, including metal-organic chemical vapor deposition (MOCVD) [12], physical vapor deposition (PVD) [13] and atomic layer deposition (ALD) [14] have been reported to realize large-area optoelectronic devices. Among these candidates, the one-step chemical vapor deposition (CVD) method has been widely used to yield high-quality and large-area MoS_2 films [15–17]. CVD-synthesized MoS_2 films allow atomically thin, uniform and large-area semiconducting properties with a direct bandgap energy of 1.9 eV and thus offer promising opportunities in high-performance wearable optoelectronics.

3.2. CVD system setup

Fig. 3.2 (a) shows the schematic illustration of the dual-heating zone CVD system for monolayer MoS_2 synthesis. In the quartz tube, two crucibles were placed. One crucible for the S powder (99.5 % Sigma Aldrich) was heated up to ~200 °C, and the other for the MoO_3 powder (99.98 % Sigma Aldrich) and the SiO_2 substrate was heated up to ~750 °C. After the growth, we could see the oval shape of grown MoS_2 films.

Fig. 3.2 (b) illustrates the photoluminescence (PL) peak-position mapping image of CVD-grown monolayer MoS_2 film with inkjet-printed Ag contacts. From the PL spectrum, the number of layers of MoS_2 can be verified at the specific point where the laser is irradiated. Hence, by this uniform blue PL peak-position mapping, the uniformity of the CVD-grown MoS_2 film could be determined.S4,S5 Furthermore, Statistical analysis of PL peak-position in both film and triangular island samples shows the strong monolayer PL peaks for both CVD-grown MoS_2 triangular islands and film. (Fig. 3.2 (c))

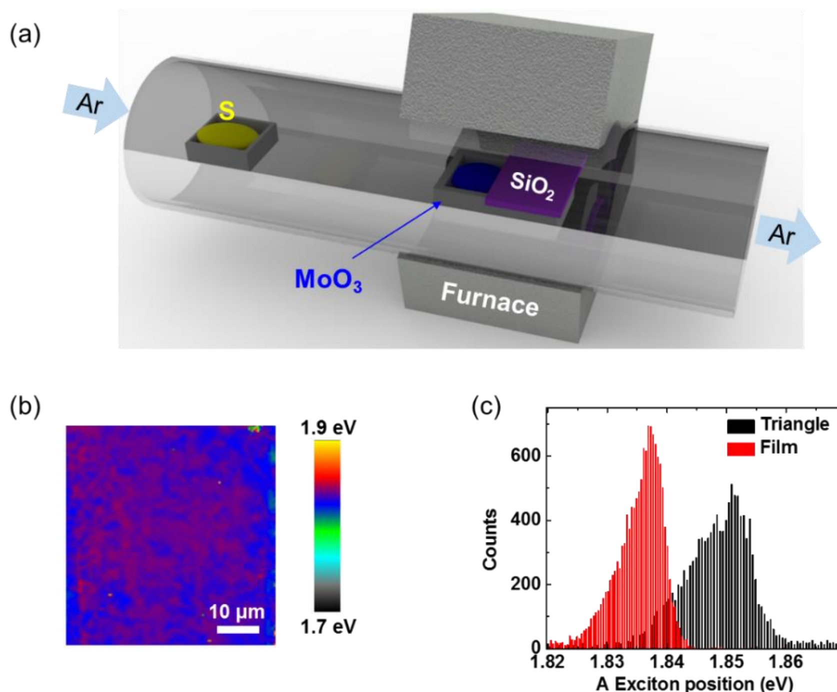

Figure 3.2 (a) MoS_2 synthesis process. (b) PL peak-position mapping of CVD-grown MoS_2 film. (c) Statistical analysis of PL peak-position in CVD-grown MoS_2 triangular island and film. Adapted from Kim *et al.* [26]

3.3. Material characterization

3.3.1. Atomic force microscopy

Fig. 3.3 (a) presents a representative optical image of a synthesized monolayer MoS_2 on a heavily-doped Si/SiO_2 substrate by a CVD system (Teraleader Co., Ltd.). In this optical image, the synthesized MoS_2 and the no-growth regions are colored dark violet and light violet, respectively. It is well-known that a large number of individual MoS_2 triangular islands that are few tenths of micrometers in size are merged into a continuous film [18] (MoS_2 triangular islands and continuous film are shown in right and left part of Fig. 3.3 (a), respectively). The thickness of the individual MoS_2 triangular islands was measured using a non-contact mode AFM (Park systems, NX 10), as shown in Fig. 3.3 (b). The cross-sectional topographic profile indicated by the cyan line included in Fig. 3.3 (b) indicates the thickness of ~0.7 nm along the blue straight line; this measurement is consistent with previously reported thickness of CVD-grown MoS_2.

3.3.2. Raman and photoluminescence

Raman and PL spectra measurements were performed on the CVD-grown MoS_2 film to clarify the spatial uniformity and the number of layers. Fig. 3.3 (c) shows Raman spectra from three different MoS_2 samples: CVD-grown MoS_2 film (red curve), MoS_2 triangular island (blue curve), and mechanically exfoliated monolayer MoS_2 flake (black curve). The CVD-grown MoS_2 triangular island and film showed similar Raman spectra with that of a mechanically exfoliated monolayer MoS_2 flake (SPI supplies, USA) on the SiO_2 (270 nm) substrate measured as a reference, including a strong Si peak at approximately 528 cm^{-1}. The expected monolayer MoS_2 Raman peak spacing of ~19.6 cm^{-1} from the out-of-plane A_{1g} (385.2 cm^{-1}) and in-plane E^1_{2g} (404.8 cm^{-1}) peaks were clearly observed on all three MoS_2 samples, as shown in the inset of Fig. 3.3 (c) [19, 20]. For further investigation, PL spectra, intensity, and peak-position mappings were measured for three different points on the CVD-grown large-area MoS_2 film. Figure 1d shows the identical strong A1 peaks around photon energy of ~1.83 eV originated from direct band-to-band recombination of excited electron-hole pairs and relatively weak B1 at approximately 2.0 eV [21–23]. The linear scale PL image of the CVD-grown MoS_2

triangular islands in inset of Figure 1d substantiates the excellent optical properties of monolayer MoS_2. The PL peak-position mapping of the CVD-grown MoS_2 film also showed good uniformity across few hundred micrometers (see Fig. 3.2) [24, 25]. These results strongly support that the CVD-grown MoS_2 film was predominantly composed of monolayers.

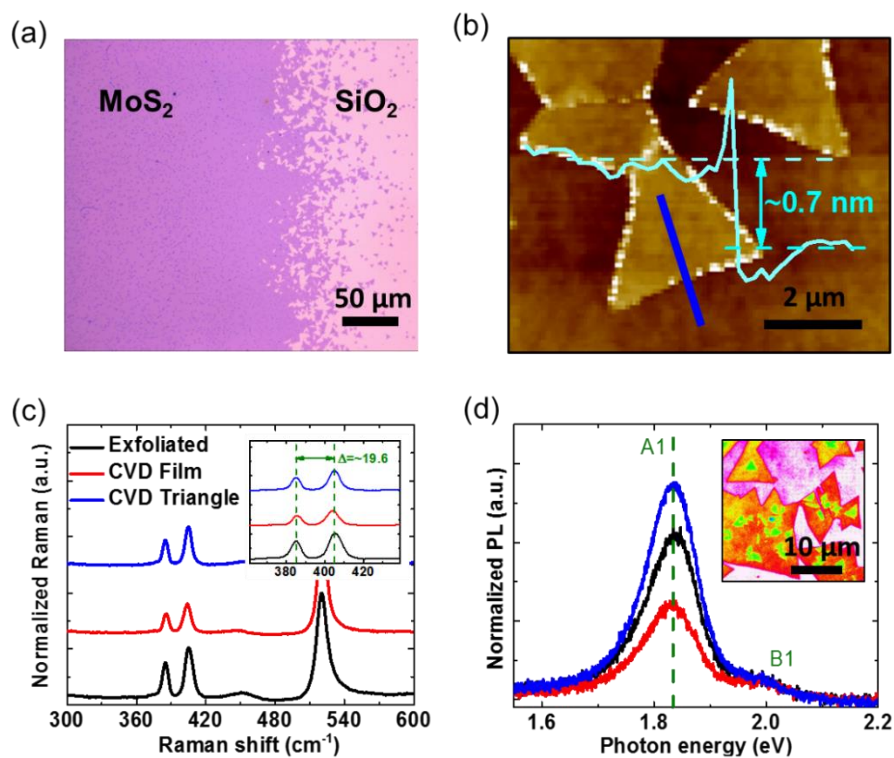

Figure 3.3 (a) Optical micrograph of CVD-grown monolayer MoS_2 (left area) and a no-growth SiO_2 (right area) substrate. (b) AFM image of CVD-grown monolayer MoS_2 triangular islands (the profile indicates the thickness of triangular islands along the blue line). (c) Raman spectra of three different MoS_2 samples. (d) PL spectra of three different points of CVD-grown films. The inset image shows linear scale PL image of triangular islands. Adapted from Kim *et al.* [26]

3.3.3. Electrical characteristics of triangular islands

The electrical properties of the monolayer MoS_2 FETs were measured in the dark in a vacuum (~10^{-3} Torr) using a semiconductor parameter analyzer (Keithley 4200, USA). Before the measurement, the MoS_2 FETs were placed on a heating stage at 400 K in a vacuum for 16 h to remove the adsorbates from the MoS_2 surface, such as water, oxygen molecules, and polymer residue. The surface adsorbates could induce charge trapping states, which can result in hysteresis in the transfer curves (drain current *versus* source-gate voltage, I_{DS}–V_{GS}) of the MoS_2 FETs [31]. No I_{DS}–V_{GS} hysteresis was observed after the heating process, which indicates the effect of surface adsorbates was negligible in this measurement.

The I_{DS}–V_{GS} characteristics (**Fig. 3.4** (c)) exhibited typical *n*-type semiconductor behavior. The field-effect mobility and on/off current ratio of the monolayer MoS_2 FETs at room temperature were found to be ~5.5 $cm^2/V{\cdot}s$ and ~10^6, respectively. The output characteristics (drain current *versus* source-drain bias, I_{DS}–V_{DS}) are displayed in the inset of Fig. 3.4 (c). Fig. 3.4 (d) shows the I_{DS}–V_{GS} curves measured in a temperature range from 80 to 300 K at a fixed V_{DS} of 0.5 V. The same transfer characteristics on the linear scale are also included in the inset. The I_{DS} decreased with decreasing temperature, indicating that the amount of thermally activated charges decreased as decreasing temperature. The fabricated CVD-grown monolayer MoS_2 FETs showed good electrical characteristics comparing to the previously reported results [21-25].

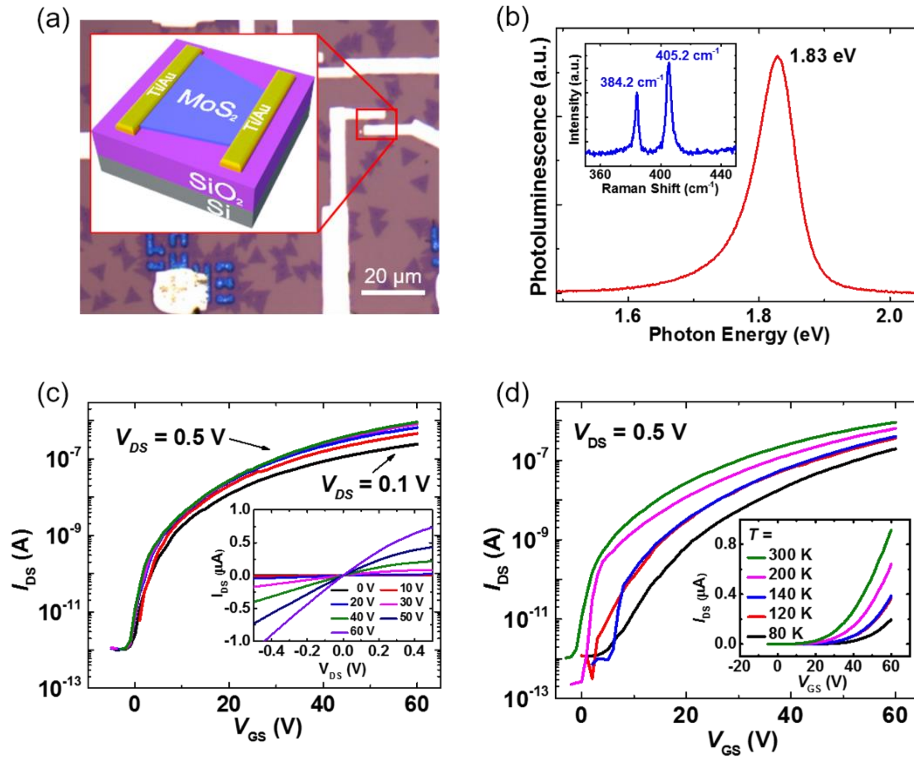

Figure 3.4 (a) Optical image showing a CVD-grown monolayer MoS_2 FET. The inset shows the schematics of the device. (b) Raman and PL spectra of a CVD-grown monolayer MoS_2. (c, d) Representative electrical characteristics of the CVD-grown monolayer MoS_2 FET. (c) I_{DS}–V_{DS} curves measured for different gate voltages at room temperature. (d) I_{DS}–V_{GS} curves measured at a fixed V_{DS} = 0.5 V for various temperatures. Adapted from Kim *et al.* [27]

3.4. Conclusion

We successfully synthesized a large-area MoS_2 film of a monolayer-thickness. Dual heating zone low-pressure CVD system was used with Ar carrying gas. The monolayer-thickness of both triangular islands and continuous films were verified by AFM, Raman and PL spectra. The electrical characteristics of the single grain CVD-grown monolayer MoS_2 island with Ti/Au top-electrodes and Si back gate were comparable to those fabricated by the mechanically exfoliated MoS_2 flakes.

References

1. Lopez-Sanchez, O.; Lembke, D.; Kayci, M.; Radenovic, A.; Kis, A. Ultrasensitive photodetectors based on monolayer MoS_2. *Nat. Nanotechnol.* **2013**, *8*, 497−501.
2. Perea-López, N.; Lin, Z.; Pradhan, N. R.; Iñiguez-Rábago, A.; Laura Elías, A.; McCreary, A.; Lou, J.; Ajayan, P. M.; Terrones, H.; Balicas, L.; Terrones, M. CVD-grown monolayered MoS_2 as an effective photosensor operating at low-voltage. *2D Mater*. **2014**, *1*, 011004.
3. Venkata Subbaiah, Y.; Saji, K.; Tiwari, A. Atomically Thin MoS_2: A Versatile Nongraphene 2D Material. *Adv. Funct. Mater*. **2016**, *26*, 2046−2069.
4. Mak, K. F.; Lee, C.; Hone, J.; Shan, J.; Heinz, T. F. Atomically Thin MoS_2: A New Direct-Gap Semiconductor. *Phys. Rev. Lett*. **2010**, *105*, 136805.
5. Splendiani, A.; Sun, L.; Zhang, Y.; Li, T.; Kim, J.; Chim, C. Y.; Galli, G.; Wang, F. Emerging Photoluminescence in Monolayer MoS_2. *Nano Lett*. **2010**, *10*, 1271−1275.
6. Lee, H. S.; Min, S.-W.; Chang, Y.-G.; Park, M. K.; Nam, T.; Kim, H.; Kim, J. H.; Ryu, S.; Im, S. MoS_2 Nanosheet Phototransistors with Thickness-Modulated Optical Energy Gap. *Nano Lett.* **2012**, *12*, 3695−3700.
7. Zhang, W.; Huang, J.-K.; Chen, C.-H.; Chang, Y.-H.; Cheng, Y.-J.; Li, L.-J. High-Gain Phototransistors Based on a CVD MoS_2 Monolayer. *Adv. Mater*. **2013**, *25*, 3456−3461.
8. Amani, M.; Lien, D.-H.; Kiriya, D.; Xiao, J.; Azcatl, A.; Noh, J.; Madhvapathy, S. R.; Addou, R.; Kc, S.; Dubey, M.; Cho, K.; Wallace, R. M.; Lee, S.-C.; He, J.-H.; Ager, J. W.; Zhang, X.; Yablonovitch, E.; Javey, A. Near-unity photoluminescence quantum yield in MoS_2. *Science* **2015**, *350*, 1065−1068.
9. Radisavljevic, B.; Radenovic, A.; Brivio, J.; Giacometti, V.; Kis, A. Single-Layer MoS_2 Transistors. *Nat. Nanotechnol*. **2011**, *6*, 147−150.
10. Castellanos-Gomez, A.; Barkelid, M.; Goossens, A. M.; Calado, V. E.; van der Zant, H. S. J.; Steele, G. Laser-Thinning of MoS_2: On Demand Generation of a Single-Layer Semiconductor. *Nano Lett*. **2012**, *12*, 3187−3192.
11. Eda, G.; Yamaguchi, H.; Voiry, D.; Fujita, T.; Chen, M.; Chhowalla, M. Photoluminescence from Chemically Exfoliated MoS_2. *Nano Lett*. **2011**, *11*, 5111−5116.
12. Kang, K.; Xie, S.; Huang, L.; Han, Y.; Huang, P. Y.; Mak, K. F.; Kim, C. J.; Muller, D.; Park, J. High-Mobility Three-Atom-Thick Semiconducting Films With Wafer-Scale Homogeneity. *Nature* **2015**, *520*, 656−660.
13. Muratore, C.; Hu, J. J.; Wang, B.; Haque, M. A.; Bultman, J. E.; Jespersen, M. L.; Shamberger, P. J.; McConney, M. E.; Naguy, R. D.; Voevodin, A. A. Continuous

Ultra-Thin MoS_2 Films Grown by Low-Temperature Physical Vapor Deposition. *Appl. Phys. Lett.* **2014**, *104*, 261604.

14. Tan, L. K.; Liu, B.; Teng, J. H.; Guo, S.; Low, H. Y.; Loh, K. P. Atomic Layer Deposition of a MoS_2 Film. *Nanoscale* **2014**, *6*, 10584−10588.
15. Lee, Y.-H.; Zhang, X.-Q.; Zhang, W.; Chang, M.-T.; Lin, C.-T.; Chang, K.-D.; Yu, Y.-C.; Wang, J. T.-W.; Chang, C.-S.; Li, L.-J.; Lin, T.-W. Synthesis of Large-Area MoS_2 Atomic Layers with Chemical Vapor Deposition. *Adv. Mater*. **2012**, *24*, 2320−2325.
16. Dumcenco, D.; Ovchinnikov, D.; Marinnov, K.; Sanchez, O. L.; Krasnozhon, D.; Chen, M.-W.; Gillet, P.; i. Morral, A. F.; Radenovic, A.; Kis, A. Large-Area Epitaxial Monolayer MoS_2. *ACS Nano* **2015**, *9*, 4611.
17. Park, W.; Baik, J.; Kim, T. Y.; Cho, K.; Hong, W. K.; Shin, H. J.; Lee, T. Photoelectron Spectroscopic Imaging and Device Applications of Large-Area Patternable Single-Layer MoS_2 Synthesized by Chemical Vapor Deposition. *ACS Nano* **2014**, *8*, 4961−4968.
18. Wang, S.; Rong, Y.; Fan, Y.; Pacios, M.; Bhaskaran, H.; He, K.; Warner, J. H. Shape Evolution of Monolayer MoS_2 Crystals Grown by Chemical Vapor Deposition. *Chem. Mater.* **2014**, *26*, 6371–6379.
19. Lee, C.; Yan, H.; Brus, L. E.; Heinz, T. F.; Hone, J.; Ryu, S. Anomalous Lattice Vibrations of Single- and Few-Layer MoS_2. *ACS Nano* **2010**, *4*, 2695–2700.
20. Zhan, Y.; Liu, Z.; Najmaei, S.; Ajayan, P. M.; Lou, J. Large-Area Vapor-Phase Growth and Characterization of MoS_2 Atomic Layers on a SiO_2 Substrate. *Small* **2012**, *8*, 966–971.
21. Mak, K. F.; Lee, C.; Hone, J.; Shan, J.; Heinz, T. F. Atomically Thin MoS_2: A New Direct-Gap Semiconductor. *Phys. Rev. Lett*. **2010**, *105*, 136805.
22. Splendiani, A.; Sun, L.; Zhang, Y. B.; Li, T. S; Kim, J.; Chim, C. Y.; Galli, G.; Wang, F. Emerging Photoluminescence in Monolayer MoS_2. *Nano Lett*. **2010**, *10*, 1271–1275.
23. Eda, G.; Yamaguchi, H.; Voiry, D.; Fujita, T.; Chen, M. W.; Chhowalla, M. Photoluminescence from Chemically Exfoliated MoS_2. *Nano Lett*. **2011**, *11*, 5111−5116.
24. Bao, W.; Borys, N. J.; Ko, C.; Suh, J.; Fan, W.; Thron, A.; Zhang, Y.; Buyanin, A.; Zhang, J.; Cabrini, S.; Ashby, P. D.; Weber-Bargioni, A.; Tongay, S.; Aloni, S.; Ogletree, D. F.; Wu, J.; Salmeron, M. B.; Schuck, P. J. Visualizing nanoscale excitonic relaxation properties of disordered edges and grain boundaries in monolayer molybdenum disulfide. *Nat. Commun*. **2015**, *6*, 7993.

25. Amani, M.; Lien, D.-H.; Kiriya, D.; Xiao, Jun.; Azcatl, A.; Noh, J.; Madhvapathy. S. R.; Addou, R.; KC, S.; Dubey, M.; Cho, K.; Wallace, R. M.; Lee, S.-C.; He, J.-H.; Ager, J. W.; Zhang, X.; Yablonovitch, E.; Javey, A. Near-unity photoluminescence quantum yield in MoS_2. Science **2015,** *350*, 1065-1068.
26. Kim, T.-Y.; Amani, M.; Ahn, G. H.; Song, Y.; Javey, A.; Chung, S.; Lee, T. Electrical Properties of Synthesized Large-Area MoS_2 Field-Effect Transistors Fabricated with Inkjet-Printed Contacts. *ACS Nano* **2016**, *10*, 2819–2826.
27. Kim, T.-Y.; Song, Y.; Cho, K.; Amani, M.; Ahn, G. H.; Kim. J.-K.; Pak, J.; Chung, S.; Javey, A.; Lee, T. Analysis of the interface characteristics of CVD-grown monolayer MoS_2 by noise measurements. *Nanotechnology*, **2017**, *28*, 145702.

4. Inkjet-printed contact electrodes on CVD-synthesized MoS_2 film

4.1. Introduction

Two-dimensional (2D) transition metal dichalcogenides (TMDCs) have attracted much attention due to their great potential monolayer applications in opto- and nanoelectronics [1–4]. Among various TMDC materials, molybdenum disulfide (MoS_2) has been most widely studied because the atomically thin (~0.65 nm) monolayer MoS_2 exhibits an excellent transparency in visible wavelength range, mechanical stiffness, flexibility, and electrical carrier mobility [5–7]. In particular, contrary to zero-bandgap graphene, MoS_2 shows a transition from indirect band gap (~1.2 eV) to direct band gap (~1.8 eV) with decreasing thickness from bulk to monolayer, which allows higher efficiency in photogeneration and recombination. Therefore, large-area monolayer MoS_2 is a promising material to use in optoelectronic devices, such as photodetectors, light-emitting-diodes (LEDs), and solar cells [8–10].

Various methods for preparation of a monolayer MoS_2, such as mechanical exfoliation, chemical exfoliation, physical vapor deposition (PVD), and chemical vapor depositions (CVD), have been recently reported [11–13]. To meet the growing demand for large-area electronics, synthetic fabrication methods to produce a large-are monolayer MoS_2 are highly desirable because a large-area monolayer MoS_2 cannot be consistently obtained using conventional mechanical or chemical exfoliation methods. Among these synthetic fabrication methods, the CVD method with molybdenum trioxide (MoO_3) and sulfur powder has enabled high-quality MoS_2 film deposition on largely selected regions and controllable thickness with excellent electrical characteristics [14–17].

For designing of source/drain (*S/D*) electrodes, electron beam (e-beam) or photo lithography techniques have been widely used on the nanometer-thick MoS_2. Unfortunately, these processes, which require unwanted procedures such as chemicals deposition, ultraviolet (UV) exposure, and contact contaminations, can degrade the electrical properties of devices and are also not suitable for large-area flexible platforms. In this regard, an inkjet-printing process, which has been

proposed for large-area, low-cost, and ambient electronics, such as organic thin-film transistors (TFTs), organic light-emitting diodes (OLEDs), oxide TFTs, and sensors, is believed to be a promising candidate for top-contact electrodes formation due to its low-cost, non-vacuum character, and large-area process abilities [18–21]. For the printed electrodes formation on monolayer MoS_2, low-cost Ag ink can be a good candidate in terms of electron-injection, because the work function of Ag (~4.26) is equivalent to that of Ti (~4.33) which is widely used as a contact metal with *n*-type semiconductor layers. To date, however, there has been no report regarding monolayer MoS_2 field-effect transistors (FETs) with inkjet-printed Ag *S/D* due to the difficulties in optimizing inkjet-printing process and compatibility between printable inks and the bottom monolayer MoS_2.

Herein, we report the demonstration of large-area monolayer MoS_2 FETs with inkjet-printed Ag *S/D* electrodes. The monolayer MoS_2 film was grown by a CVD system, and the Ag electrodes were inkjet-printed using a commercial drop-on-demand (DOD) printer, which allows for the realization of large-area and low-cost electronics. The metallic ink for the *S/D* formation was carefully selected by considering the wetting and contact properties of the underlying MoS_2 film. The predominantly monolayer character of the CVD-grown MoS_2 film was verified by atomic force microscopy (AFM), Raman, and photoluminescence (PL) spectroscopy measurements. The electrical properties of the MoS_2 FETs with the printed *S/D,* including field-effect mobility and on/off ratio, were comparable to those of the FETs with conventionally deposited contacts using e-beam or photo lithography processes. The wetting and contact properties between the Ag contacts and the MoS_2 semiconductor layer were also investigated by extracting the surface energy and the contact resistance. Moreover, the electrical instability of the MoS_2 FET was investigated under a prolonged positive gate-bias stress to verify the charge-trapping mechanism between the CVD-grown monolayer MoS_2 and the SiO_2 gate dielectric. This study for the integration with large-area CVD grown monolayer MoS_2 films and low-cost inkjet-printed contacts can have a strong impact in the fields of 2D TMDC nano and optoelectronics.

4.2. Experiments

4.2.1. Inkjet-printing process

For S/D electrodes formation, a nanoparticle-type Ag ink containing 32 wt.% Ag (DGP 40LT-15C, ANP Co. Ltd.) and a cartridge which ejects 1 picoliter (pl) of ink droplets were used. After the Ag ink was inkjet-printed at a drop velocity of 8 m/s and a drop spacing of 30 μm onto a 60 °C substrate using DMP-2831 (Fuji Films Corp.) printer, the sample was sintered on a 180 °C hot-plate for 30 min under atmospheric environment. Note that the no more oxidation related degradations during other fabrication processes or measurements are not observed because the surface of printed Ag conductive layers is slightly oxidized during the sintering process [55].

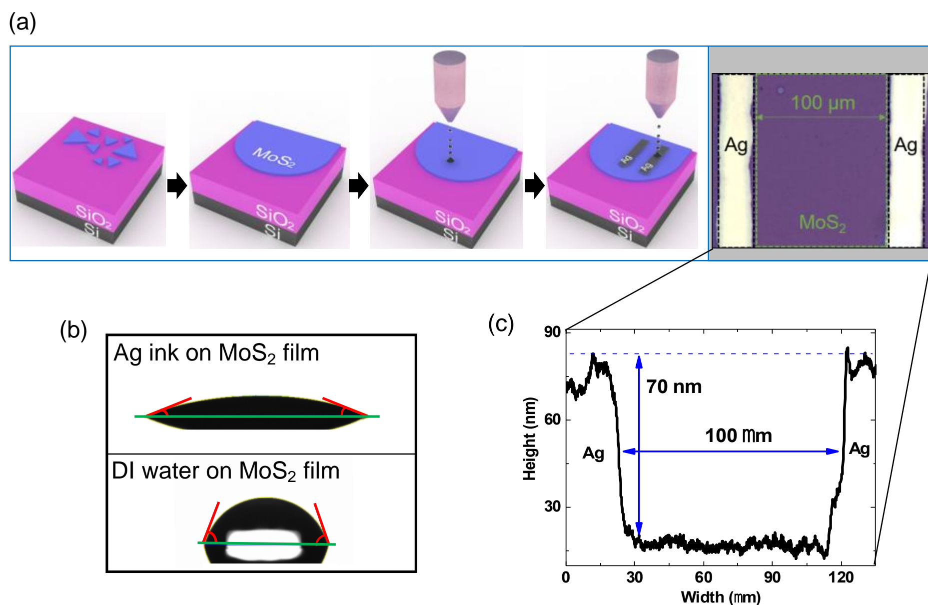

Figure 4.1 (a) Schematic illustrations and a representative optical image (in grey background) of the fabrication of CVD-grown monolayer MoS_2 FETs with inkjet-printed Ag electrodes. (b) Representative optical images of sessile drops on CVD-grown monolayer MoS_2 film. The top and bottom images show the Ag ink and DI water drops on the MoS_2 film, respectively. (c) The surface profiles of CVD-grown monolayer MoS_2 films with inkjet-printed Ag electrodes. Adapted from Kim *et al.* [55]

4.3. Results and discussions

4.3.1. Electrical characteristics

The electrical properties were characterized using a semiconductor parameter analyzer (4155C, Agilent Technologies) under ambient condition. In particular, all measurements were performed in a dark box to avoid the contribution of the photocurrent in the CVD-grown MoS_2 FETs [33, 34]. Figure 3a shows the transfer characteristics (drain-source current *versus* gate-source voltage, I_{DS}–V_{GS}) measured for drain-source voltage (V_{DS}) ranging from 1 to 20 V by sweeping V_{GS} from -40 to 60 V. The results showed the typical n-type semiconductor behavior with a field-effect mobility (μ_{FE}) of 1.8 cm^2/V·s and on/off ratio of over 10^4 at V_{DS} of 1 V. The inset in **Fig. 4.2** (a) shows the logarithmic scale plot of the transfer characteristics. Considering the reported μ_{FE} values of 1 to 45 cm^2/V·s for CVD-grown monolayer MoS_2 FETs at room temperature [35], several factors are believed to deteriorate the μ_{FE} of the devices in this study. The electrical characteristics measurements performed in ambient condition would cause lower charge transport due to oxygen or water absorption on the semiconductor surface that can deplete electrons, resulting in the degradation of the channel conductivity [36, 37]. In addition, intrinsic structural defects in CVD-grown MoS_2 films, such as grain boundaries and point defects, and the interfacial states between the MoS_2 layer and SiO_2 surface could limit the charge transport as well [35, 38, 39]. The electrical properties can, therefore, be improved by optimizing the structural quality of the CVD-grown monolayer MoS_2, employing passivation layers onto the channel, and transferring the CVD-grown MoS_2 films onto dangling-bond free hexagonal boron nitride (hBN) substrates to minimize the interfacial traps [40, 42]. However, the key advantage of a use of inkjet-printed Ag contacts on a large-area CVD-grown MoS_2 film lies not on the electrical performance improvement but on the low-cost drop-on-demand (DOD) deposition.

Fig. 4.2 (b) shows the output characteristics (drain-source current *versus* drain-source voltage, I_{DS}–V_{DS}) measured at V_{GS} ranging from –20 to 20 V in increments of 10 V by sweeping V_{DS} from 0 to 20 V. The output characteristics revealed good linearity at low V_{DS} regime. In the relationship $I_{DS} \propto {V_{DS}}^{\gamma}$ in the logarithmic scale plot, as shown in Fig. 4.2 (c), the average γ (= linearity parameter) values of ~1.1

was found to be close to 1, indicating the formation of an ohmic contact between the CVD-grown MoS_2 film and the printed Ag electrodes. For further investigation, the contact resistance values between the channel and the printed *S/D* was also extracted because the contact properties strongly affect the electrical characteristics [7, 43].

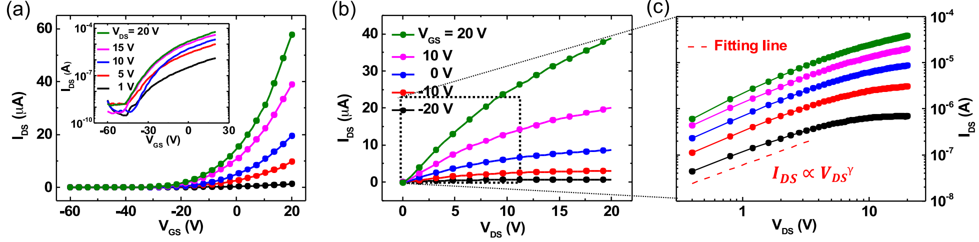

Figure 4.2 Representative electrical characteristics of the CVD-grown monolayer MoS_2 FET with the inkjet-printed Ag electrodes. (a) Transfer characteristics (I_{DS}–V_{GS}) measured at different V_{DS}. The inset figure shows the same transfer characteristics on a log scale. (b) Output characteristics (I_{DS}–V_{DS}) measured at different V_{GS}. (c) Log-Log plot of output characteristics in low V_{DS} region. The red dashed lines indicate the fitting line to the $I_{DS} \propto V_{DS}^{\gamma}$ relationship. Adapted from Kim *et a*. [55]

4.3.2. Y-function method and contact resistances

Although transmission line measurement, also called transfer length method (TLM), is widely used to evaluate contact resistance of FETs, it cannot be conveniently employed because several transistors with various channel lengths and uniform contacts are necessary to extract the accurate value. Due to these limitations, the Y-function method (YFM) was proposed for the contact resistance extraction between the CVD-grown monolayer MoS_2 FET and the Ag printed contacts, as shown in **Fig. 4.3** (a). YFM has been widely used to analyze the contact resistance and intrinsic mobility (μ_0) in the low V_{DS} linear regime ($V_{GS} - V_{th} >> V_{DS}$) for both organic and carbon nanotube based FETs [44–47]. Recently, Chang et al. reported that YFM can also be a robust method to extrapolate the contact resistances of nanometer-thick MoS_2 FETs.[48] Generally, I_{DS} in a linear region can be described by

$$I_{DS} = \frac{W}{L} C_i \mu_{eff} (V_{GS} - V_{th}) V_{DS} = \frac{W}{L} C_i \frac{\mu_0}{1+\theta(V_{GS}-V_{th})} (V_{GS} - V_{th}) V_{DS} \quad (3)$$

where μ_{eff}, μ_0, C_i, V_{th}, W, L, and θ denote the effective mobility in linear regime; the intrinsic mobility; the capacitance between the channel and the gate per unit area; the threshold voltage; the channel width; the channel length; and the mobility attenuation coefficient, respectively. According to the definition of transconductance ($g_m=\partial I_{DS}/\partial V_{GS}$), the Y-function can be defined as

$$Y \equiv \frac{I_{DS}}{\sqrt{g_m}} = \sqrt{I_{DS}}\sqrt{(V_{GS}-V_{th})\{1+\theta(V_{GS}-V_{th})\}} = \sqrt{\mu_0 C_i V_{DS}\frac{W}{L}}\,(V_{GS}-V_{th}) \quad (4)$$

From the slope of Y-function, the extrapolated μ_0 value at $V_{DS} = 1$ V, which is independent of the attenuating factors, was 2.1 $cm^2/V{\cdot}s$, which is 17 % bigger than the measured μ_{FET} of 1.8 $cm^2/V{\cdot}s$. The mobility attenuation factor θ can be described by the following equation:

$$\theta = \theta_{ch} + \theta_c = \theta_{ch} + \mu_0 C_i R_C \frac{W}{L} \quad (5)$$

where θ_{ch}, θ_c, and R_C denote the mobility attenuation factor from the channel, such as a surface roughness and phonon scattering; mobility attenuation factor from the contact; and the contact resistance, respectively. Assuming that θ_{ch} is negligible [44, 48, 50], the value of θ is ~0.02 and the contact resistance of 115 kΩ can be extracted at high V_{GS} from the slope of Y-function (the red dashed line in Fig. 4.3 (a)). The contact resistance value is relatively higher than the reported contact resistance values of the MoS_2 devices fabricated with various methods. But these contact resistance values cannot be compared fairly due to the several reasons (see the detailed discussion in the Supporting Information).

The extracted contact resistance is also consistent with the saturated total resistance of 175 kΩ at sufficiently large V_{DS} and V_{GS} where the contribution of the contact resistance is much more dominant than that of the channel (Fig. 4.3 (b)). This contact resistance value is higher than the reported values [49–51], because unwanted residues from the organic solvent or ligands may limit charge injection from the contacts to the MoS_2 layer during the metallic ink sintering process. In addition, the quite porous surface of the printed *S/D* due to the size of Ag nanoparticles (~35 nm) results in smaller effective-contact areas. In particular, increasing evidence has suggested that metal/MoS_2 junction formations depend on not only metal work function but also the chemical reactions at the metal/MoS_2 [7, 43]. Thus, the contact property of inkjet-printed Ag electrodes on CVD-grown MoS_2

would be different from that of evaporated ones, thus affecting the electrical characteristics of the devices.

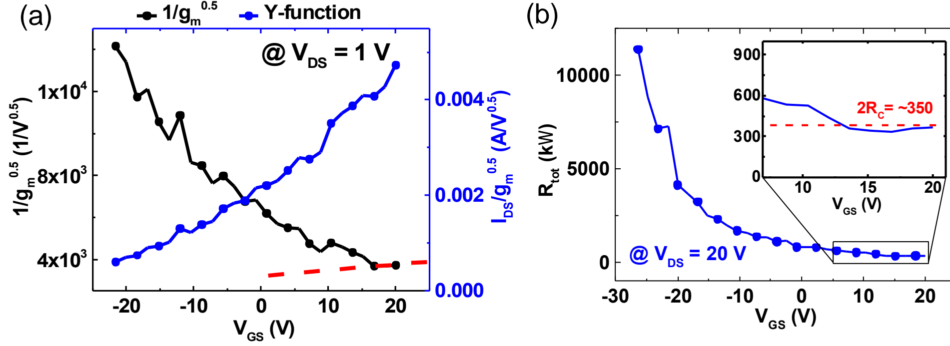

Figure 4.3 (a) $1/\sqrt{g_m}$ and Y-function ($I_{DS}/\sqrt{g_m}$)of the CVD-grown monolayer MoS_2 FET with inkjet-printed electrodes at V_{DS} of 1 V. (b) Graph of the total resistance (R_{tot}) *versus* V_{GS} graph at V_{DS} of 20 V; the enlarged image shows the R_{tot} at V_{GS} from 5 to 20 V. The red dashed line shows the slope around V_{DS} of 15 V. Adapted from Kim *et al*. [55]

4.3.3. Electrical instability and gate-bias stress effect

The electrical instability was also investigated by measuring the electrical characteristics of the FETs under positive gate-bias stress of 30 V. The transfer characteristics were measured every 500 s for 10,000 s at V_{DS} of 20 V by sweeping V_{GS} from –40 to 60 V while interrupting the gate-bias stress. **Figs. 4.4** (a) and (b) show the transfer curves on the logarithmic and linear scales, respectively. The curves shifted in the positive gate-bias direction as a function of applied gate-bias stress time. The subthreshold swing (*S.S.*) and slope of the curves were almost identical to during the measurement (the inset of Fig. 4.4 (b)). These results support that the defect-creation of extra electron trapping states is negligible, whereas the trapped electrons at the MoS_2/SiO_2 interface or bulk dielectric that can reduce the effective gate-bias are dominant for the V_{th} instability during positive gate-bias stress. The stress time dependence of the V_{th} shift during a prolonged gate-bias was fitted to the stretched-exponential equation described as

$$V_{th} = \Delta V_0 \left[1 - \exp(-\left(\frac{t_{st}}{\tau}\right)^{\beta})\right] \quad (6)$$

where ΔV_0, τ, β, and t_{st} denote the change of V_{th} after infinite time, the characteristic trapping time, the stretched-exponent, and the gate-bias stress time, respectively (**Fig. 4.4** (c)). The stretched-exponential equation has been developed to quantitatively model the charge trapping mechanism by injection of carriers from the channel to the near-interface or the bulk dielectric in amorphous silicon (*a*-Si) TFTs [52]. The extrapolated values of ΔV_0, τ, and β were found to be ~18.1 V, 8.1 × 10^2 sec, and ~ 0.413, respectively. The statistical coefficient R^2 value of 0.9937 indicates that experimental data (black closed circles) were well fitted to the stretched-exponential equation fitting line (as the statistical coefficient R^2 is closed to 1, the experimental data are well-fitted to the equation). Notably, the larger τ value compared to that of the mechanically exfoliated MoS_2 FETs [53] indicates the higher trap density in the CVD-grown MoS_2 film or at the interface with the dielectric and also can be evidence of a large number of band tail states of the CVD-grown monolayer MoS_2 film [54].

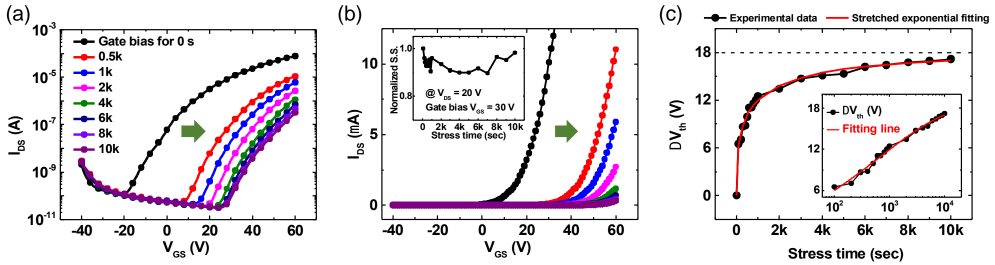

Figure 4.4 Transfer characteristics measured in ambient with respect to the different gate-bias stress time up to 10,000 sec on (a) log and (b) linear scales. The gate-bias stress voltage V_{GS} was 30 V. The inset of (b) shows the change of normalized subthreshold swing (S.S.) with respect to the stress time. (c) Threshold voltage shift (ΔV_{th}) with respect to the value of pre-stress curve. The solid red line represents a stretched-exponential fitting to the experimental data using equation (7). The inset figure shows the ΔV_{th} on a log scale. Adapted from Kim *et al.* [55]

4.4. Conclusion

In summary, we report the large-area CVD-grown MoS_2 FETs fabricated with low-cost inkjet-printed Ag S/D electrodes and their electrical properties. The CVD-grown monolayer MoS_2 films showed well-defined and uniform Raman and PL spectra, and the inkjet-printed S/D electrodes were deposited successfully onto the MoS_2 films without any surface treatments by optimizing the printing process. The large-area FETs showed comparable electrical characteristics to those of MoS_2 FETs with conventionally deposited contacts at room temperature under ambient condition. The contact property between the MoS_2 and printed Ag electrodes was also analyzed using the Y-function method. Furthermore, the charge-trapping mechanism was primarily responsible for the electrical instability, especially the V_{th} shift, of CVD-grown monolayer MoS_2 FETs under positive gate-bias stress. This study provides a promising pathway for integrating CVD-grown large-area monolayer MoS_2 FETs with a low-cost inkjet-printing technique.

References

1. Jariwala, D.; Sangwan, V. K.; Lauhon, L. J.; Marks, T. J.; Hersam, M. C. Emerging Device Applications for Semiconducting Two-Dimensional Transition Metal Dichalcogenides. *ACS Nano* **2014**, *8*, 1102-1120.
2. Fiori, G.; Bonaccorso, F.; Iannaccone, G.; Palacios, T.; Neumaier, D.; Seabaugh, A.; Banerjee, K. S.; Colombo, L. Electronics Based on Two-Dimensional Materials. *Nat. Nanotechnol.* **2014**, *9*, 768-779.
3. Wu, S.; Buckley, S.; Schalbley, R. J.; Feng, L.; Yan, J.; Mandrus, G. D.; Hatami, F.; Yao, W.; Vučković, J.; Majumdar, A.; Xu, X. Monolayer Semiconductor Nanocavity Lasers with Ultralow Thresholds. *Nature* **2015**, *520*, 69-72.
4. Duan, X.; Wang, C.; Pan, W.; Yu, R.; Duan, X.; Few-Layer MoS_2: Two-Dimensional Transition Metal Dichalcogenides as Atomically Thin Semiconductors: Opportunities and Challenges. *Chem. Soc. Rev.* **2015**, *44*, 8859-8876.
5. Radisavljevic, B.; Radenovic, A.; Brivio, J.; Giacometti, V.; Kis, A. Single-Layer MoS_2 Transistors. *Nat. Nanotechnol*. **2011**, *6*, 147–150.
6. Ganatra, R.; Zhang, Q. Few-layer MoS_2: A Promising Layered Semiconductor. *ACS Nano* **2014**, *8*, 4074−4099.
7. Schmidt, H.; Giustiniano, F.; Eda, G. Electronic Transport Properties of Transition Metal Dichalcogenide Field-Effect Devices: Surface and Interface Effects. *Chem. Soc. Rev*. **2015**, *44*, 7715−7736.
8. Wang, Q. H.; Kalantar-Zadeh, K.; Kis, A.; Coleman, J. N.; Strano, M. S. Electronics and Optoelectronics of Two-Dimensional Transition Metal Dichalcogenides. *Nat. Nanotechnol*. **2012**, *7*, 699–712.
9. Tsai, M.-L.; Su, S.-H.; Chang, J.-K.; Tsai, D.-S.; Chen, C.-H.; Wu, C.-I.; Li, L.-J.; Chen, L.-J.; He, J.-H. Monolayer MoS_2 Hetero-junction Solar Cells. *ACS Nano* **2014**, *8*, 8317–8322.
10. Li, D.; Cheng, R.; Zhou, H.; Wang, C.; Yin, A.; Chen, Y.; Weiss, N. O.; Huang, Y.; Duan, X. Electric-Field-Induced Strong Enhancement of Electroluminescence in Multilayer Molybdenum Disulfide. *Nat. commun.* **2015,** *6*, 7509.
11. Muratore, C.; Hu, J. J.; Wang, B.; Haque, M. a.; Bultman, J. E.; Jespersen, M. L.; Shamberger, P. J.; McConney, M. E.; Naguy, R. D.; Voevodin, A. A. Continuous Ultra-Thin MoS_2 Films Grown by Low-Temperature Physical Vapor Deposition. *Appl. Phys. Lett*. **2014**, *104*, 261604–5.
12. Lukowski, M. A.; Daniel, A. S.; Meng, F.; Forticaux, A.; Li, L.; Jin, S. Enhanced Hydrogen Evolution Catalysis from Chemically Exfoliated Metallic MoS_2 Nanosheets. *J. Am. Chem. Soc.* **2013**, *135*, 10274−10277.

13. Lee, Y.-H.; Zhang, X.-Q.; Zhang, W.; Chang, M.-T.; Lin, C.-T.; Chang, K.-D.; Yu, Y.-C.; Wang, J. T.-W.; Chang, C.-S.; Li, L.-J.; et al. Synthesis of Large-Area MoS_2 Atomic Layers with Chemical Vapor Deposition. *Adv. Mater*. **2012**, *24*, 2320– 2325.
14. van der Zande, A. M.; Huang, P. Y.; Chenet, D. A.; Berkel- bach, T. C.; You, Y.; Lee, G.-H.; Heinz, T. F.; Reichman, D. R.; Muller, D. A.; Hone, J. C. Grains and Grain Boundaries in Highly Crystalline Monolayer Molybdenum Disulphide. *Nat. Mater*. **2013**, *12*, 554–561.
15. Wang, X. S.; Feng, H. B.; Wu, Y. M.; Jiao, L. Y. Controlled Synthesis of Highly Crystalline MoS_2 Flakes by Chemical Vapor Deposition. *J. Am. Chem. Soc*. **2013**, *135*, 5304–5307.
16. Kang, K.; Xie, S.; Huang, L.; Han, Y.; Huang, P. Y.; Mak, K. F.; Kim, C.-J.; Muller, D.; Park, J. High-Mobility Three-Atom-Thick Semiconducting Films with Wafer-Scale Homogeneity. *Nature* **2015**, *520*, 656–660.
17. Han, G. H.; Kybert, N. J.; Naylor, C. H.; Lee, B. S.; Ping, J.; Park, J. H.; Kang, J.; Lee, S. Y.; Lee, Y. H.; Agarwal, R.; et al. Seeded Growth of Highly Crystalline Molybdenum Disulphide Monolayers at Controlled Locations. *Nat. Commun*. **2015**, *6*, 6128.
18. Lau, P. H.; Takei, K.; Wang, C.; Ju, Y.; Kim, J.; Yu, Z.; Takahashi, T.; Cho, G.; Javey, A. Fully Printed, High Performance Carbon Nanotube Thin-Film Transistors on Flexible Substrates. *Nano Lett*. **2013**, *13*, 3864−3869.
19. Chung, S.; Jang, M.; Ji, S.-B.; Im, H.; Seong, N.; Ha, J.; Kwon, S.-K.; Kim, Y.-H.; Yang, H.; Hong, Y. Flexible High-Performance All-Inkjet-Printed Inverters: Organo-Compatible and Stable Interface Engineering. *Adv. Mater.* **2013,** *25*, 4773-4777.
20. Søndergaard, R. R.; Hösel, M.; Krebs, F. C. Roll-to-Roll fabrication of large area functional organic materials. *J. Polym. Sci., Part B: Polym. Phys*. **2013**, *51*, 16−34.
21. Secor, E. B.; Hersam, M. C. Emerging Carbon and Post-Carbon Nanomaterial Inks for Printed Electronics. *J. Phys. Chem. Lett*. **2015**, *6*, 620−626.
22. Wang, S.; Rong, Y.; Fan, Y.; Pacios, M.; Bhaskaran, H.; He, K.; Warner, J. H. Shape Evolution of Monolayer MoS_2 Crystals Grown by Chemical Vapor Deposition. *Chem. Mater.* **2014**, *26*, 6371–6379.
23. Lee, C.; Yan, H.; Brus, L. E.; Heinz, T. F.; Hone, J.; Ryu, S. Anomalous Lattice Vibrations of Single- and Few-Layer MoS_2. *ACS Nano* **2010**, *4*, 2695–2700.
24. Zhan, Y.; Liu, Z.; Najmaei, S.; Ajayan, P. M.; Lou, J. Large-Area Vapor-Phase Growth and Characterization of MoS_2 Atomic Layers on a SiO_2 Substrate. *Small* **2012**, *8*, 966–971.
25. Mak, K. F.; Lee, C.; Hone, J.; Shan, J.; Heinz, T. F. Atomically Thin MoS_2: A New Direct-Gap Semiconductor. *Phys. Rev. Lett*. **2010**, *105*, 136805.

26. Splendiani, A.; Sun, L.; Zhang, Y. B.; Li, T. S; Kim, J.; Chim, C. Y.; Galli, G.; Wang, F. Emerging Photoluminescence in Monolayer MoS_2. *Nano Lett*. **2010**, *10*, 1271–1275.
27. Eda, G.; Yamaguchi, H.; Voiry, D.; Fujita, T.; Chen, M. W.; Chhowalla, M. Photoluminescence from Chemically Exfoliated MoS_2. *Nano Lett*. **2011**, *11*, 5111−5116.
28. Bao, W.; Borys, N. J.; Ko, C.; Suh, J.; Fan, W.; Thron, A.; Zhang, Y.; Buyanin, A.; Zhang, J.; Cabrini, S.; Ashby, P. D.; Weber-Bargioni, A.; Tongay, S.; Aloni, S.; Ogletree, D. F.; Wu, J.; Salmeron, M. B.; Schuck, P. J. Visualizing nanoscale excitonic relaxation properties of disordered edges and grain boundaries in monolayer molybdenum disulfide *Nat. Commun*. **2015**, *6*, 7993.
29. Amani, M.; Lien, D.-H.; Kiriya, D.; Xiao, Jun.; Azcatl, A.; Noh, J.; Madhvapathy. S. R.; Addou, R.; KC, S.; Dubey, M.; Cho, K.; Wallace, R. M.; Lee, S.-C.; He, J.-H.; Ager, J. W.; Zhang, X.; Yablonovitch, E.; Javey, A. Near-unity photoluminescence quantum yield in MoS_2. Science **2015,** *350*, 1065-1068.
30. Van Oss, C. J.; Chaudhury, M. K.; Good, R. J. Interfacial Lifshitz-van der Waals and Polar Interactions in Macroscopic Systems. *Chem. Rev*. **1988**, *88*, 927.
31. Van oss, C. J.; Good, R. J.; Chaudhury, M. K. Additive and Nonadditive Surface Tension Components and The Interpretation of Contact Angles. *Langmuir* **1988**, *4*, 884.
32. Gaur, A. P. S.; Sahoo, S.; Ahmadi, M.; Dash, S. P.; Guinel, M. J.- F.; Katiyar, R. S. Surface Energy Engineering for Tunable Wettability through Controlled Synthesis of MoS_2. *Nano Lett*. **2014**, *14*, 4314−4321.
33. Lin, J.; Li, H.; Zhang, H.; Chen, W. Plasmonic Enhancement of Photocurrent in MoS_2 Field-Effect-Transistor. *Appl. Phys. Lett*. **2013**, *102*, 203109−3.
34. Lopez-Sanchez, O.; Lembke, D.; Kayci, M.; Radenovic, A.; Kis, A. Ultrasensitive Photodetectors Based on Monolayer MoS_2. *Nat. Nanotechnol*. **2013**, *8*, 497–501.
35. Hong, J. H.; Hu, Z. X.; Probert, M.; Li, K.; Lv, D. H.; Yang, X. N.; Gu, L.; Mao, N. N.; Feng, Q. L.; Xie, L. M. Exploring Atomic Defects in Molybdenum Disulphide Monolayers. *Nat. Commun*. **2015**, *6*, 6293.
36. Late, D. J.; Liu, B.; Matte, H. S. S. R.; Dravid, V. P.; Rao, C. N. R. Hysteresis in Single-Layer MoS_2 Field Effect Transistors. *ACS Nano* **2012**, *6*, 5635–5641.
37. Qiu, H.; Pan, L. J.; Yao, Z. N.; Li, J. J.; Shi, Y.; Wang, X. R. Electrical Characterization of Back-Gated Bi-layer MoS_2 Field-Effect Transistors and the Effect of Ambient on Their Performances. *Appl. Phys. Lett*. **2012**, *100*, 123104−3.
38. Najmaei, S.; Amani, M.; Chin, M. L.; Liu, Z.; Birdwell, A. G.; O'Regan, T. P.; Ajayan, P. M.; Dubey, M.; Lou, J. Electrical Transport Properties of Polycrystalline Monolayer Molybdenum Disulfide. *ACS Nano* **2014**, *8*, 7930–7937.
39. Dumcenco, D.; Ovchinnikov, D.; Marinov, K.; Lazić. P.; Gibertini, M.; Marzari, N.;

Sanchez, O. L.; Kung, Y.-C.; Krasnozhon, D.; Chen, M.-W.; Bertolazzi, S.; Gillet, P.; Fontcuberta i Morral, A.; Radenovic, A.; Kis. A. Large-Area Epitaxial Monolayer MoS_2. *ACS Nano* **2015**, *9*, 4611–4620.

40. Yu, Z. H.; Pan, Y. M.; Shen, Y. T.; Wang, Z. L.; Ong, Z. Y.; Xu, T.; Xin, R.; Pan, L. J.; Wang, B. G.; Sun, L. T. Towards Intrinsic Charge Transport in Monolayer Molybdenum Disulfide by Defect and Interface Engineering. *Nat. Commun*. **2014**, *5*, 5290.
41. Lee, G.-H.; Yu, Y.-J.; Cui, X.; Petrone, N.; Lee, C.-H.; Choi, M. S.; Lee, D.-Y.; Lee, C.; Yoo, W. J.; Watanabe, K.; et al. Flexible and Transparent MoS_2 Field-Effect Transistors on Hexagonal Boron Nitride-Graphene Heterostructures. *ACS Nano* **2013**, *7*, 7931–7936.
42. Bao, W.; Cai, X.; Kim, D.; Sridhara, K.; Fuhrer, M. S. High Mobility Ambipolar MoS_2 Field-Effect Transistors: Substrate and Dielectric Effects. *Appl. Phys. Lett*. **2013**, *102*, 042104−4.
43. McDonnell, S.; Addou, R.; Buie, C.; Wallace, R. M.; Hinkle, C. L. Defect-Dominated Doping and Contact Resistance in MoS_2. *ACS Nano* **2014**, *8*, 2880–2888.
44. Ghibaudo, G.; New Method for the Extraction of MOSFET Parameters. *Electron. Lett*. **1988**, *24*, 543–545.
45. Fleury, D.; Cros, A.; Brut, H.; Ghibaudo, G. In *New Y-Function-Based Methodology for Accurate Extraction of Electrical Parameters on Nano-Scaled MOSFETs, IEEE International Conference on Microelectronic Test Structures*, ICMTS 2008; March 24-27, 2008; IEEE: New York, **2008**; pp 160-165.
46. Xu, Y.; Minari, T.; Tsukagoshi, K.; Chroboczek, J. A.; Ghibaudo, G. Direct Evaluation of Low-Field Mobility and Access Resistance in Pentacene Field-Effect Transistors. *J. Appl. Phys*. **2010**, *107*, 114507–7.
47. Choi, S.-J.; Bennett, P.; Takei, K.; Wang, C.; Lo, C. C.; Javey, A.; Bokor, J. Short-Channel Transistors Constructed with Solution-Processed Carbon Nanotubes. *ACS Nano* **2013**, *7*, 798−803.
48. Chang, H.-Y.; Zhu, W.; Akinwande, D. On the Mobility and Contact Resistance Evaluation for Transistors Based on MoS_2 or Two-Dimensional Semiconducting Atomic Crystals. *Appl. Phys. Lett*. **2014**, *104*, 113504–5.
49. Kappera, R.; Voiry, D.; Yalcin, S. E.; Branch, B.; Gupta, G.; Mohite, A. D.; Chhowalla, M. Phase-Engineered Low-Resistance Contacts for Ultra-thin MoS_2 Transistors. *Nat. Mater.* **2014**, *13*, 1128–1134.
50. Kwon, H.-J.; Jang, J.; Kim, S.; Subramanian, V.; Grigoropoulos, C. P. Electrical characteristics of multilayer MoS_2 transistors at real operating temperatures with different ambient conditions. *Appl. Phys. Lett*. **2014**, *105*, 152105–5.

51. Na, J.; Shin, M.; Joo, M.-K.; Huh, J.; Jeong Kim, Y.; Jong Choi, H.; Hyung Shim, J.; Kim, G.-T. Separation of Interlayer Resistance in Multilayer MoS_2 Field-Effect Transistors. *Appl. Phys. Lett*. **2014**, *104*, 233502–5.
52. Libsch, F. R.; Kanicki, J. Bias-Stress-Induced Stretched-Exponential Time-Dependence of Charge Injection and Trapping in Amorphous Thin-Film Transistors. *Appl. Phys. Lett*. **1993**, *62*, 1286–1288.
53. Yang, S.; Park, S.; Jang, S.; Kim, H.; Kwon, J.-Y. Electrical Stability of Multilayer MoS_2 Field-Effect Transistor under Negative Bias Stress at Various Temperatures. *Phys. Status Solidi RRL* **2014**, *8*, 714-718.
54. Zhu, W.; Low, T.; Lee, Y.-H.; Wang, H.; Farmer, D. B.; Kong, J.; Xia, F.; Avouris, P. Electronic Transport and Device Prospects of Monolayer Molybdenum Disulphide Grown by Chemical Vapour Deposition. *Nat. Commun*. **2014**, *5*, 3087.
55. Kim, T.-Y.; Amani, M.; Ahn, G. H.; Song, Y.; Javey, A.; Chung, S.; Lee, T. Electrical Properties of Synthesized Large-Area MoS_2 Field-Effect Transistors Fabricated with Inkjet-Printed Contacts. *ACS Nano* **2016**, *10*, 2819–2826.

5. Fully flexible and transparent MoS_2 phototransistor with inkjet-printed components

5.1. Introduction

Molybdenum disulfide (MoS_2) has shown many interesting features, such as a finite energy band gap and good electrical mobility in its atomically thin two-dimensional (2D) form. Therefore, researches on a sub-thermioninc band-to-band tunneling transistors or near-ideal quantum yield were reported using atomically thin MoS_2 channels. To make full use of its unique optical and electrical merits, synthesis of large and uniform monolayer MoS_2 is highly required. Herein, chemical vapor deposition (CVD) technique has been highly investigated to produce large and uniform monolayer MoS_2. Generally, electron-beam nanolithography or photolithography techniques are used to design the contact electrodes on the atomically thin MoS_2 channel. Unfortunately, these processes involve unwanted procedures, such as chemical deposition of photoresist and ultraviolet exposure, which could be a reason of contact contaminations. Moreover, it is inadequate for large-area flexible platform. In this regard, an inkjet-printing process, which has been proposed for large-area area, low-cost, and ambient electronics, is believed to be a promising candidate for top-contact electrode formation due to its low-cost, non-vacuum character, and large-area process abilities. Low-cost and drop-on-demand (DOD) inkjet-printing technique allows for the realization of large-area and low-cost electronics.

In this work, we will report a demonstration of fully flexible and transparent FETs based on CVD-grown large monolayer MoS_2 channel layer with all inkjet-printed components. First, the monolayer MoS_2 film (up to ~1 cm^2) were synthesized by CVD system under low pressure conditions. The uniform structure of MoS_2 film were verified by Raman and photoluminescene (PL) spectra and mapping. Subsequently, the CVD-grown monolayer MoS_2 film was transferred onto a flexible polyethylene naphthalate (PEN) substrate and all the other device components including contact electrodes and top dielectric layers were fabricated by inkjet-printing technique without any surface treatment under ambient conditions. This

integration of an atomically thin large area MoS_2 synthesis and DOD inkjet-printing technique is highly meaningful, because it allows the fabrication of fully transparent and flexible devices directly onto the plastic substrate. The top-gated FET devices have shown high transparency at the wavelength of 400-800 nm and the electrical characteristics were preserved with repetitive bending tests. In addition, our devices have shown reasonable photoswitching properties such as a photoresponsivity of ~0.1 $W \cdot A^{-1}$ and an external quantum efficiency of ~8 %, comparable to the MoS2 devices fabricated by conventional methods (such as e-beam deposition of metal electrodes or atomic layer deposition of dielectric layers). We believe that the fully transparent and flexible top-gated FET with CVD-grown monolayer MoS_2 and all inkjet-printed components could be an essential milestone in flexible optoelectronic applications of atomically thin transition metal dichalcogenide (TMDC) materials.

5.2. Experiments

5.2.1. Device fabrication process

Fig. 5.1 shows the device fabrication process. The monolayer MoS_2 film was CVD-grown on SiO_2/Si (270 nm) substrates (Fig. 5.1 (b)). A large-area monolayer MoS_2 film was synthesized with MoO_3 and sulfur (S) powders in the presence of Ar carrier gas [1]. The heating temperatures were 700 °C and 200 °C for MoO_3 and S powders, respectively.The synthesized MoS_2 was patterned using reactive ion etching (RIE) in an O_2 plasma while covered with a shadow mask to form the channel layers (Fig. 5.1 (c)). The patterned CVD-synthesized MoS_2 film was transferred onto a polyethylene-naphthalate (PEN) substrate using the poly(methyl methacrylate) (PMMA)-assisted transfer method [2]. After attaching thermal tape as a supporting layer, the entire structure (supporting tape/PMMA/MoS_2/SiO_2/Si) was immersed in a potassium hydroxide solution (~25 %) to detach the MoS_2 film from the SiO_2/Si substrate. After a PMMA supporting layer was deposited by spin-coating on MoS_2/SiO_2 (Fig. 5.1 (e)), a REVALPHA thermal tape (Nitto Denko, Japan) was attached as a supporting layer. Then, the whole structure (tape/PMMA/MoS_2/SiO_2) was immersed into a potassium hydroxide (KOH) solution (~25 %) at 70 °C to detach the tape/PMMA/MoS_2 structure from the SiO_2/Si substrates (Fig. 5.1 (f)). The tape/PMMA/MoS_2 structure was placed onto the PEN substrate using IPA as an

adhesion promoter, and then the PMMA supporting layer was carefully removed (Fig. 5.1 (g)). Finally, the PEDOT:PSS electrodes and PVP dielectric layers were directly inkjet-printed without surface treatment (Figs. 5.1 (h)–(k)). Specifically, poly (3,4-ethylenedioxythiophene) polystyrene sulfonate (PEDOT:PSS) source/drain (S/D) electrodes, a cross-linked poly(4-vinylphenol) (PVP) gate dielectric layer and a PEDOT:PSS top-gate electrode were sequentially inkjet-printed on the desired positions of the device substrate. The maximum processing temperature of 180 °C facilitated the direct integration of a wide range of printable organic materials onto the flexible substrate. It should be noted that the ultra-thin MoS_2 channel layer was extremely sensitive to the surface roughness of underlying layers; therefore, a top-gate configuration was employed in this work because of the relatively poor surface roughness of the inkjet-printed PVP gate dielectric (rms roughness of ~4 nm) compared with that of the PEN substrate (rms roughness of ~1 nm).

5.2.2. Light illumination setup

Monochromatic lasers with wavelengths of 405, 520, 650, and 780 nm were used (MDE5240V, Su Semiconductor) to investigate the photocharacteristics. All electrical characteristics of our MoS_2 phototransistors were measured using a semiconductor parameter analyser (Keithley 4200) and an individual monochromatic light with intensities ranging from 0.1-1000 W/m^2.

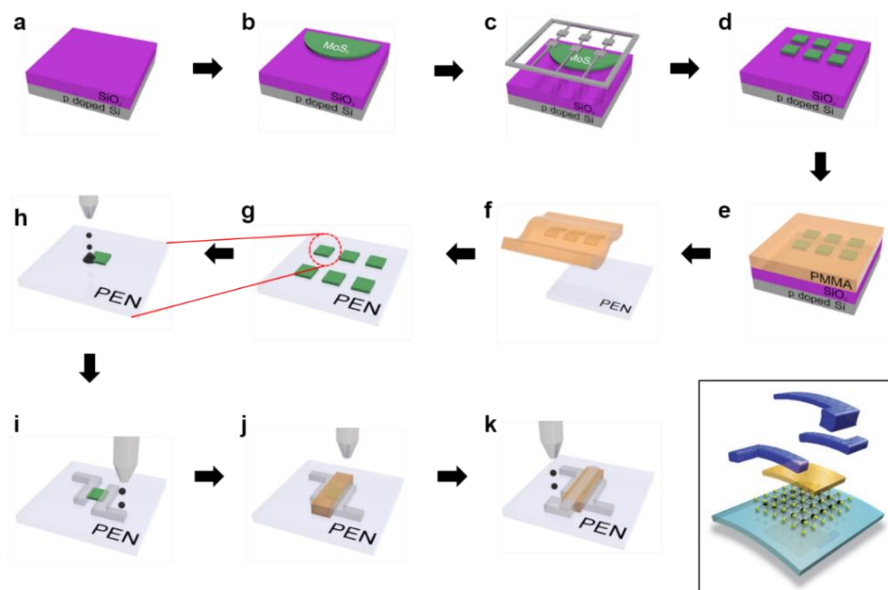

Figure 5.1 (a) Cleaned the SiO_2/Si substrate. (b) CVD-grown MoS_2 on the SiO_2/Si substrate. (c) MoS_2 patterning process using RIE while covered with a shadow mask. (d) Clearly patterned monolayer MoS_2 film. (e) Spin-coated the PMMA supporting layer onto MoS_2/SiO_2. (f) After detaching the monolayer MoS_2 film from SiO_2 using a KOH solution, the MoS_2/PMMA structure was placed on the PEN substrate. (g) Transferred the MoS_2 onto the PEN substrate. Direct inkjet-printing of (h-i) PEDOT:PSS *S/D* electrodes, (j) PVP dielectric layer and (k) PEDOT:PSS gate electrodes. Adapted from Kim *et al.* [30]

5.2.3. Optical transmittance of the device

The fully printed phototransistors exhibited good transparency (over ~76 %) in the visible wavelength range (from 400-800 nm), whereas a PEN substrate exhibited a transmittance of 87 % in the same wavelength range (**Fig. 5.2** (a))

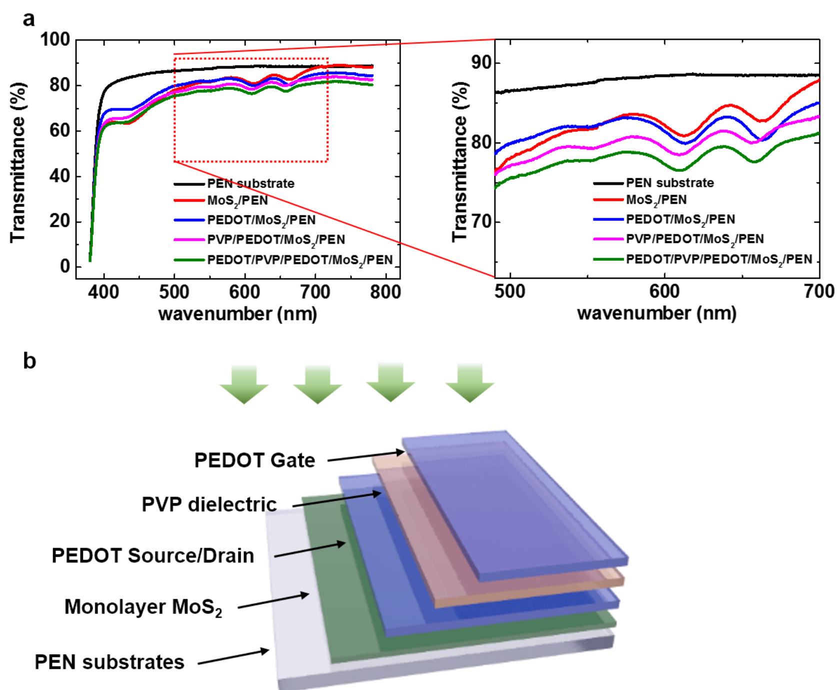

Figure 5.2 (a) Transmittance spectra of the layer-by-layer stacked device structures from the bare PEN substrate to fully stacked structures (PEDOT:PSS/PVP/PEDOT:PSS/MoS_2/PEN films). (b) Schematic of the stacked structures. Adapted from Kim *et al.* [30]

5.3. Results and discussions

5.3.1. Fully-printed MoS_2 phototransistors

The contact properties of the PEDOT:PSS and PVP inks on the MoS_2 film and PEN substrate were optimized with a consideration of the ink chemistry that allowed well-defined printed layers while preventing undesirable dewetting issues on the underlying layers (**Fig. 5.3** (b)). Owing to the use of ultra-thin MoS_2 and transparent organic layers, the fully integrated phototransistors exhibited high transparency (Fig. 5.3 (c)). Photographic images of our devices are shown on a piece of paper (left, Fig. 5.3 (c)) and in front of a building (right, Fig. 5.3 (c)). In particular, the laser-light transmitted the entire device structure without reflection or scattering (Fig. 5.3 (d)).

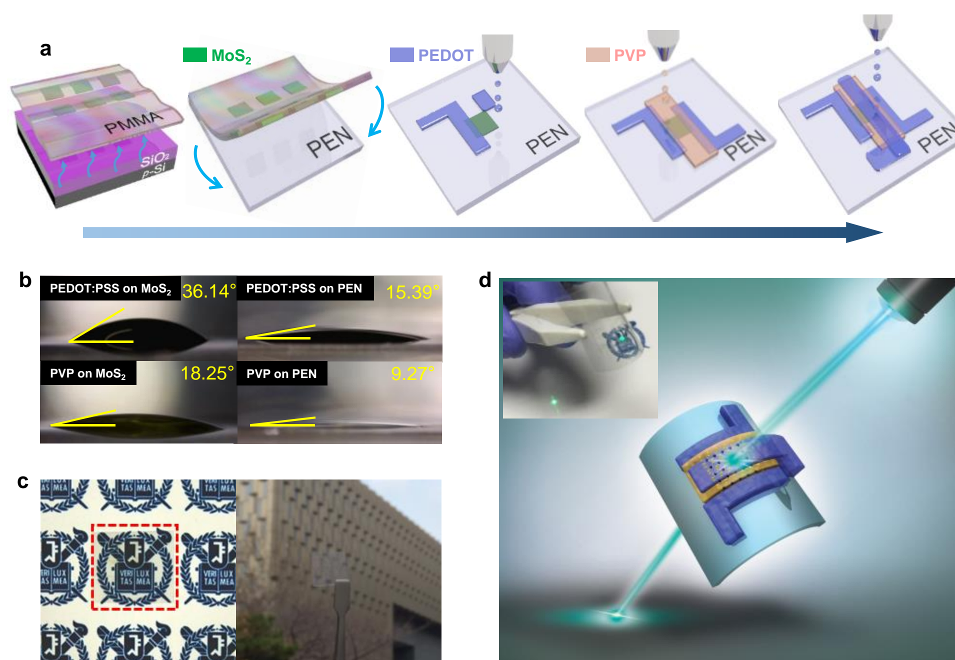

Figure 5.3 (a) Schematic illustration of the fabrication processes for fully printed, flexible and transparent CVD-synthesized MoS_2 phototransistors. (b) Contact angle measurements of PEDOT:PSS (top) and PVP (bottom) ink on the MoS_2 film (left) and PEN substrate (right). (c) Digital images of the transparent MoS_2 phototransistor arrays. In the left image, the device arrays (marked with a red square) were placed on a piece of paper with university symbols. The right image was taken in front of a building. (d) Photographic image (inset) and schematic of the devices under laser illumination. Adapted from Kim *et al.* [30]

5.3.2. Characteristics of CVD-grown monolayer MoS_2 film

The uniformity of the synthesized monolayer MoS_2 film on a SiO_2/Si substrate was evaluated by Raman and photoluminescence (PL) spectroscopy techniques. The Raman peak difference (~20.7 cm^{-1}) between in-plane E^1_{2g} and out-of-plane A_{1g} (**Fig. 5.4** (a)) and a distinct PL peak A (~670 nm; ~1.85 eV) at the K point of the Brillouin zone (Fig. 5.4 (b)) provided evidence that the CVD-synthesized MoS_2 film is an uniformly grown monolayer [3–5]. Interestingly, the blueshifted PL signal of the transferred MoS_2 film on the PEN substrate was observed due to a slight tensile strain that was induced in the MoS_2 layer during the CVD synthesis process because of the difference in thermal expansion coefficients of the SiO_2/Si and MoS_2 layers [6, 7]. For the further investigation, PL mapping over an area of 20 μm × 20 μm was performed, as shown in the inset of Fig. 5.4 (b). The color distribution indicated that the CVD-synthesized MoS_2 channel layer has uniform bandgap energy at 1.85 eV. Cross-sectional scanning transmission electron microscopy (STEM) with energy dispersive X-ray spectroscopy (EDS) also supported that the MoS_2 layer was uniformly synthesized showing confined Mo and S signals (Fig. 5.4 (c)). To implement phototransistor arrays, the MoS_2 film was selectively patterned using RIE in an O_2 plasma (Fig. 5.4 (d)). Note that the CVD-synthesized monolayer MoS_2 film typically has a dark violet color on 270 nm-thick SiO_2 [1, 5, 8]. The white-dashed rectangles indicate the patterned MoS_2 channels after the RIE process. By exploiting the optimized PMMA-assisted transfer method, the patterned CVD-synthesized MoS_2 array was successfully transferred onto a PEN substrate without physical damage. The transferred patterned MoS_2 array films on the PEN substrate maintained its structural quality (Fig. 5.4 (b) and (e)); however, relatively weak PL and X-ray photoelectron spectroscopy (XPS) signals were observed because of light scattering from the PEN substrates. The XPS spectra depicted in Fig. 5.4 € indicate the binding energies of the Mo 3d and S 2p orbitals (229.9, 233, 162.6 and 163.9 eV for Mo $3d_{5/2}$, Mo $3d_{3/2}$, S $2p_{3/2}$ and S $2p_{1/2}$, respectively). The difference between the binding energies of each orbital (3.1 eV and 1.3 eV for Mo 3d and S 2p, respectively) were consistent with the previously reported values [1] of CVD-synthesized monolayer MoS_2. In addition, the S/Mo atomic ratio of 1.95 estimated from the XPS,

suggests that our synthesized MoS_2 film is stoichiometric. The lower binding energy of transferred MoS_2 film originated from the transferring process.

The fully printed MoS_2 phototransistors with organic materials showed a high transmittance over 76 % in the visible wavelength range, whereas the bare PEN substrate exhibited a transmittance of ~87 % in the same wavelength range (Fig. 5.4 (f)). Noticeable absorption peaks at 1.87 eV and 2.02 eV (marked as arrows) were observed. These peaks were attributed to the direct transition from the spin-orbit split valence band to the conduction band of MoS_2 monolayer, which is consistent with the previously reported results for both mechanically exfoliated [9, 10] and CVD-synthesized MoS_2 monolayers [11]. The PEDOT:PSS and PVP layers evenly reduced the optical transmittance by ~5 % over the whole visible range. Because the fully transparent printed organic layers do not exhibit specific absorption peaks in the visible wavelength range, the photocharacteristics were entirely determined by the atomically thin MoS_2 channel layer without interference (Fig. 5.2). To consider the worst-case in transmittance, the measured films were prepared by sequentially printing all phototransistor layers over the entire PEN substrate in following order: MoS_2, PEDOT:PSS, PVP and PEDOT:PSS on the PEN substrate (see the inset illustration of Fig. 5.4 (f) and Fig. 5.2). Inset shows the schematic of the stacked layers (PEDOT:PSS/PVP/PEDOT:PSS/MoS_2/PEN) of our devices.

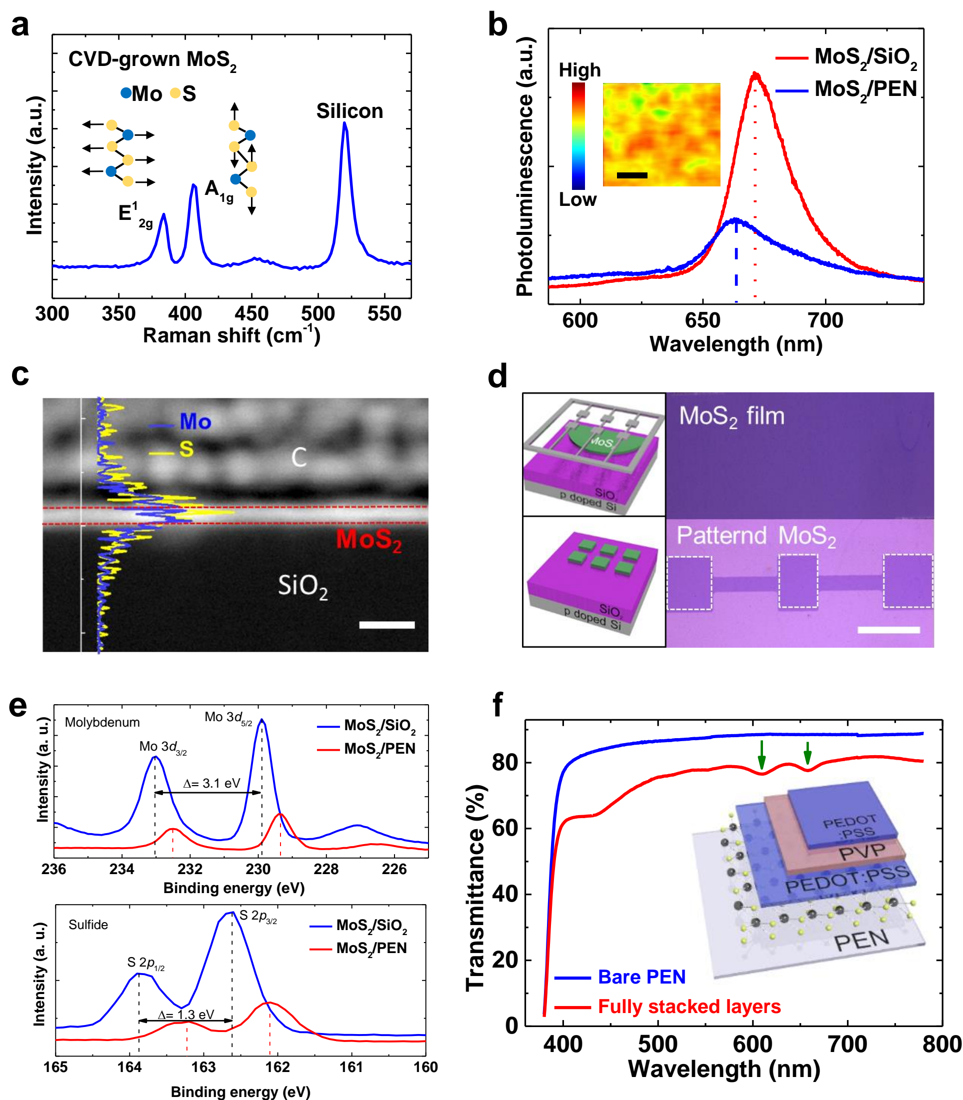

Figure 5.4 (a) Raman spectrum of a CVD-synthesized monolayer MoS_2 film on a SiO_2/Si substrate. (b) PL spectra of CVD-synthesized monolayer MoS_2 films on SiO_2/Si and PEN substrates. The inset shows a PL intensity mapping at 670 nm (= 1.85 eV). Scale bar is 5 μm. (c) EDS data of Mo (blue line) and S (yellow line) and a cross-sectional STEM image of a CVD-synthesized MoS_2 film on a SiO_2/Si substrate. Scale bar is 5 nm. (d) Optical images of a CVD-synthesized MoS_2 channel before (top) and after (bottom) selective patterning processes. Scale bar is 400 μm. (e) XPS spectra of a CVD-synthesized monolayer MoS_2 film on a SiO_2/Si (top) substrate and transferred MoS_2 film on the PEN (bottom) substrate. (f) Transmittance spectra of a bare PEN substrate (blue line) and fully stacked films (red line). Adapted from Kim *et al.* [30]

5.3.3. Electrical characteristics under bent conditions

Fig. 5.5 (a) exhibits the transfer (source drain current versus gate voltage, I_{DS}–V_{GS}) characteristics of a fully printed MoS_2 phototransistor measured in air. In particular, the gate leakage (I_{GS}), which can cause significant interference in the photocurrent [12], was greatly suppressed by removing the PMMA supporting layer very carefully and optimizing the inkjet-printing conditions for the PVP dielectric layer formation. These efforts were necessary because the hydrophobic PMMA residue causes a critical dewetting issue during the PVP printing process, resulting in a high gate to source leakage current. As a result, the gate leakage current was drastically suppressed to < 1 nA after removing the PMMA layer with the optimized steps. The extracted field-effect mobility in the linear regime (μ) was found to be ~0.27 cm^2/V·s using the following equation, $\mu = \left(\frac{\partial I_{DS}}{\partial V_{GS}}\right)\frac{L}{W}\frac{1}{C_i V_{DS}}$, where $\frac{\partial I_{DS}}{\partial V_{GS}}$, L, W, C_i and V_{DS} denote the transconductance, channel length, channel width, capacitance between the channel and gate per unit area and source-drain voltage, respectively. The grain boundaries of the CVD-synthesized MoS_2 film [13], the low-conductivity of the PEDOT:PSS electrode, and the low-k PVP dielectric deteriorated the electrical performance of the fully printed CVD-grown MoS_2 phototransistors. Although the difference in the electron affinity of monolayer MoS_2 (~4.0 eV) and the work function of the printed PEDOT:PSS layer (~5.07 eV) , resulted in a high Schottky barrier, an ohmic-like contact property was exhibited with a good linearity of I_{DS} near low V_{DS} due to the chemical reactions at the PEDOT:PSS/MoS_2 interfaces [14]. Furthermore, It should be noted that because the large-area MoS_2 channel also had a relatively high resistance due to the long-channel length of ~100 μm and large number of MoS_2 grain boundaries on the film [8], which resulted in an on-state current of ~10^{-7} A, the contact resistance of PEDOT:PSS with the MoS_2 channel (~1.9 MΩ determined from the Y-function method [15]) was acceptable [16, 17].

Owing to the use of soft organic materials, the electrical performance was not degraded during a mechanical stability test over 1,000 repetitive bending-relaxation cycles at a bending radius (R) of 5 mm, which corresponds to a uniaxial tensile strain of 1.26 % along the channel length (Fig. 5.5 (b)). The atomically thin MoS_2 layer allowed superior durability under a mechanical strain of 11 % compared with widely used engineering materials, such as carbon nanotubes and oxide-based

semiconductors [18, 19]. In contrast to the good mechanical stability under repetitive bending cycles, the μ and subthreshold swing (*SS*) measured in a bent state (*R* of 15 mm, 11 mm, 7.5 mm, and 5 mm) increased as *R* decreased. These enhancements can be attributed to a reduction in the band gap energy of CVD-synthesized MoS_2 when mechanically deformed [18, 20, 21, 22].

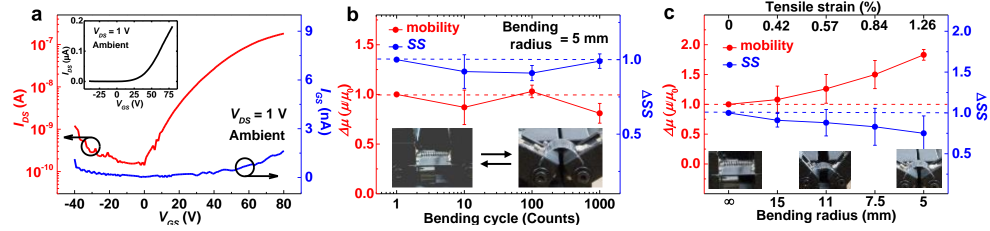

Figure 5.5 (a) I_{DS}–V_{GS} curves using a log scale at V_{DS} = 1 V. Inset represents the I_{DS}–V_{GS} curves using a linear scale. The change in mobility (μ) and subthreshold swing (*SS*) versus (b) number of bending cycles with a bending radius = 5 mm and (c) bending radii of 5, 7.5, 11, 15 and ∞. Adapted from Kim *et al.* [30]

5.3.4. Photo-characteristics

Fig. 5.6 shows the photocharacteristics of the MoS_2 phototransistors under laser illumination. The measurements were executed after the devices were maintained on a 400 K hot-chuck in vacuum for 20 h to provide successfully suppressed I_{GS} by eliminating adsorbed water and oxygen molecules on the MoS_2 and gate dielectric layers. To investigate the contribution of the photocurrent ($I_{light} = I_{ph} + I_{dark}$) to I_{DS}, the ratio of I_{light} to I_{dark} in ON and OFF states was measured for different wavelengths with a fixed laser power density of 717 W/m^2 at V_{DS} = 10 V (Figure 4a). Under laser illumination, the ratio in the OFF state drastically increased from ~10^1 to ~10^4, whereas in the ON state, the ratio was below 10 (see the blue-shaded region in Fig. 5.6 (a)) [23]. An increase in the large I_{ph} in the OFF state was observed in our study compared with that of the previously reported phototransistors with mechanically exfoliated MoS_2 due to the relatively large channel area (W/L = 400 μm/100 μm) [24]. This advantage of CVD-synthesized MoS_2 offers opportunities for large-area optoelectronics applications with a good photosensitivity. Moreover, the ratio of currents in the ON and OFF states also showed good linearity in the laser power

density (ranging from 0.43 to 717 W/m^2 at λ = 520 nm), which is an important characteristic for photosensor applications (Fig. 5.6 (b)).

The photodecay time (τ_{decay}), which depends on V_{GS}, was also investigated by measuring the time-resolved photocurrent before and after laser illumination for 20 s with V_{GS} values of -40 V, 0 V and 40 V at λ = 520 nm (Fig. 5.6 (c)). The decay curves were fitted by a stretched exponential equation, $I_{DS} = I_{ph,intial} exp\left[-\left(\frac{t}{\tau}\right)^{\beta}\right]$, where $I_{ph,initial}$, t, β and τ denote I_{dark}, time, the fitting parameter and relaxation time, respectively. After laser illumination with a power density of 717 W/m^2, τ_{decay} decreased from 6.7 s to 1.7 s as V_{GS} increased from -40 V to 40 V because the photocurrent contribution was weak at high V_{GS}, as previously mentioned. The shorter decay time compared with that of conventional CVD-synthesized MoS_2 phototransistors fabricated on a SiO_2/Si substrate is attributed to fewer interfacial traps between printed PVP dielectric and transferred MoS_2 layers [23, 24]. The monotonic decrease in responsivity with increasing incident photopower indicates that the trap states of CVD-synthesized MoS_2 are saturated (Fig. 5.6 (d)) [25, 26].

The responsivity and detectivity were also characterized for various laser wavelengths (Fig. 5.6 (e)). The fully transparent MoS_2 phototransistors exhibited comparable photoresponsivity and photodetectivity over the entire visible range from 400 to 800 nm compared with that of mechanically exfoliated MoS_2 phototransistors on opaque platforms [27–29]. Moreover, the wavelength-dependent external quantum efficiency (EQE) (up to ~6.6 %) also supports the fully printed transparent phototransistors, which exhibit good photocharacteristics, even though a top-gate configuration was employed (Fig. 5.6 (f)) [29]. Note that the wavelength-dependent EQE is dominantly attributed to the absorbance peaks in the MoS_2 layer (Fig. 5.2).

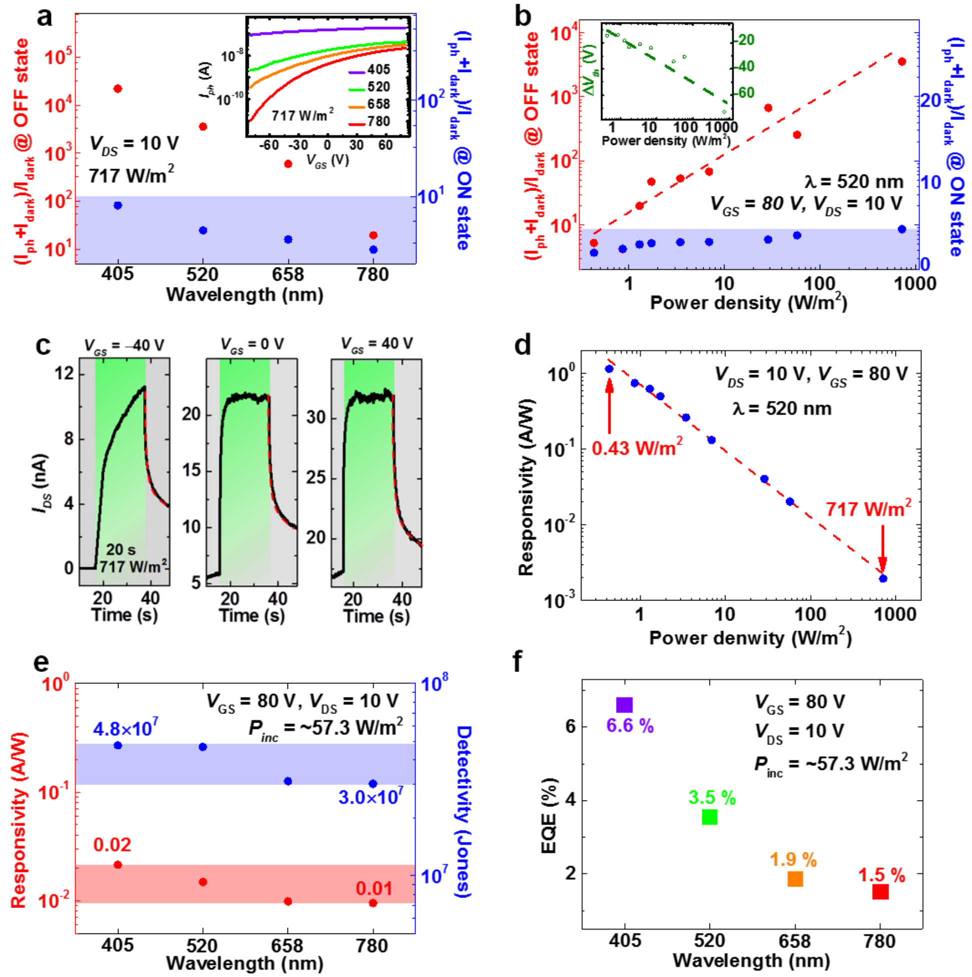

Figure 5.6 (a) The ratio of I_{light} (= I_{ph} + I_{dark}) to I_{dark} in the ON and OFF states as a function of a) wavelength and (b) laser power at a fixed V_{DS} = 10 V. Insets of (a) and (b) exhibit I_{ph} versus V_{GS} and the change in V_{th} with respect to the laser power, respectively. As the laser power increased, V_{th} shifted in the negative voltage direction, which indicates an increase in I_{ph} in the subthreshold regime. (c) Time-resolved photocurrent measurement under laser illumination (λ = 520 nm). The green-shaded regions indicate laser illumination for 20 s. (d) Responsivity of phototransistors as a function of power density under laser illumination (λ = 520 nm). (e) Photoresponsivity, photodetectivity and (f) external quantum efficiency as a function of wavelength at a fixed V_{GS} = 80 V, V_{DS} = 10 V and laser power density = 57.3 W/m^2. Adapted from Kim *et al.* [30]

5.4. Conclusion

In summary, we have successfully demonstrated fully printed, transparent MoS_2 phototransistor arrays on flexible platforms. The CVD-synthesized monolayer MoS_2 and organic dielectric and electrode components were deposited directly onto flexible substrates using the optimized polymer-assisted transfer and inkjet-printing technologies, respectively. By employing ultra-thin MoS_2 and transparent organic layers, the fully printed phototransistors exhibited excellent transparency and tolerance while maintaining electrical characteristics under tensile strain. Our work presents a new opportunity to realize 2D TMDC-based low-cost wearable device applications beyond conventional electronics that employ brittle components.

References

1. Park, W.; Baik, J.; Kim, T. Y.; Cho, K.; Hong, W. K.; Shin, H. J.; Lee, T. Photoelectron Spectroscopic Imaging and Device Applications of Large-Area Patternable Single-Layer MoS_2 Synthesized by Chemical Vapor Deposition. *ACS Nano* **2014**, *8*, 4961−4968.
2. Jiao, L. Y.; Fan, B.; Xian, X. J.; Wu, Z. Y.; Zhang, J.; Liu, Z. F. Creation of Nanostructures with Poly(methyl methacrylate)-Mediated Nanotransfer Printing. *J. Am. Chem. Soc*. **2008**, *130*, 12612–12613.
3. Mak, K. F.; Lee, C.; Hone, J.; Shan, J.; Heinz, T. F. Atomically Thin MoS_2: A New Direct-Gap Semiconductor. *Phys. Rev. Lett*. **2010**, *105*, 136805.
4. Splendiani, A.; Sun, L.; Zhang, Y.; Li, T.; Kim, J.; Chim, C. Y.; Galli, G.; Wang, F. Emerging Photoluminescence in Monolayer MoS_2. *Nano Lett*. **2010**, *10*, 1271−1275.
5. Schmidt, H.; Wang, S.; Chu, L.; Toh, M.; Kumar, R.; Zhao, W.; Castro Neto, A. H.; Martin, J.; Adam, S.; Ö zyilmaz, B.; Eda, G. Transport Properties of Monolayer MoS_2 Grown by Chemical Vapor Deposition. *Nano Lett*. **2014**, *14*, 1909−1913.
6. Amani, M.; Chin, M. L.; Mazzoni, A. L.; Burke, R. A.; Najmaei, S.; Ajayan, P. M.; Lou, J.; Dubey, M. Growth-substrate induced performance degradation in chemically synthesized monolayer MoS_2 field effect transistors. *Appl. Phys. Lett*. **2014**, *104*, 203506.
7. Conley, H. J.; Wang, B.; Ziegler, J. I.; Haglund, R. F.; Pantelides, S. T.; Bolotin, K. I. Bandgap engineering of strained monolayer and bilayer MoS_2. *Nano Lett*. **2013**, *13*, 3626−3630.
8. Kim, T.-Y.; Amani, M.; Ahn, G. H.; Song, Y.; Javey, A.; Chung, S.; Lee, T. Electrical Properties of Synthesized Large-Area MoS_2 Field-Effect Transistors Fabricated with Inkjet-Printed Contacts. *ACS Nano* **2016**, *10*, 2819–2826.
9. Mak, K. F.; Lee, C.; Hone, J.; Shan, J.; Heinz, T. F. Atomically Thin MoS_2: A New Direct-Gap Semiconductor. *Phys. Rev. Lett*. **2010**, *105*, 136805.
10. Splendiani, A.; Sun, L.; Zhang, Y.; Li, T.; Kim, J.; Chim, C. Y.; Galli, G.; Wang, F. Emerging Photoluminescence in Monolayer MoS_2. *Nano Lett*. **2010**, *10*, 1271−1275.
11. Mukherjee, B.; Tseng, F.; Gunlycke, D.; Kumar, K.; Eda, G.; Simsek, E. Complex electrical permittivity of the monolayer molybdenum disulfide (MoS_2) in near UV and visible. *Opt. Mater. Express* **2015**, *5*, 447−455.
12. Yu, W. J.; Liu, Y.; Zhou, H.; Yin, A.; Li, Z.; Huang, Y.; Duan, X. Highly efficient gate-tunable photocurrent generation in vertical heterostructures of layered materials *Nat. Nanotechnol.* **2013**, *8*, 952−958.
13. Dumcenco, D.; Ovchinnikov, D.; Marinnov, K.; Sanchez, O. L.; Krasnozhon, D.; Chen, M.-W.; Gillet, P.; i. Morral, A. F.; Radenovic, A.; Kis, A. Large-Area Epitaxial Monolayer MoS_2. *ACS Nano* **2015**, *9*, 4611.

14. McDonnell, S.; Addou, R.; Buie, C.; Wallace, R. M.; Hinkle, C. L. Defect-Dominated Doping and Contact Resistance in MoS_2. *ACS Nano* **2014**, *8*, 2880−2888.
15. Chang, H.-Y.; Zhu, W.; Akinwande, D. On the mobility and contact resistance evaluation for transistors based on MoS_2 or two-dimensional semiconducting atomic crystals. *Appl. Phys. Lett*. **2014**, *104*, 113504.
16. Sirringhaus, H.; Kawase, T.; Friend, R. H.; Shimoda, T.; Inbasekaran, M.; Wu, W.; Woo, E. P. High-Resolution Inkjet Printing of All-Polymer Transistor Circuits. *Science* **2000**, *290*, 2123−2126.
17. Lee, M. W.; Lee, M. Y.; Choi, J. C.; Park, J. S.; Song, C. K. Fine patterning of glycerol-doped PEDOT:PSS on hydrophobic PVP dielectric with ink jet for source and drain electrode of OTFTs. *Org. Electron*. **2010**, *11*, 854−859.
18. Bertolazzi, S.; Brivio, J.; Kis, A. Stretching and Breaking of Ultrathin MoS_2. *ACS Nano* **2011**, *5*, 9703−9709.
19. Park, K.; Lee, D.; Kim, B.; Jeon, H.; Lee, N.; Whang, D.; Lee, H.; Kim, Y.; Ahn, J.-H. Stretchable, Transparent Zinc Oxide Thin Film Transistors. *Adv. Funct. Mater*. **2010**, *20*, 3577–3582.
20. Wu, W.; Wang, L.; Li, Y.; Zhang, F.; Lin, L.; Niu, S.; Chenet, D.; Zhang, X.; Hao, Y.; Heinz, T. F.; Hone, J.; Wang, Z. L. Piezoelectricity of single-atomic-layer MoS_2 for energy conversion and piezotronics. *Nature* **2014**, *514*, 470−474.
21. Conley, H. J.; Wang, B.; Ziegler, J. I.; Haglund, R. F.; Pantelides, S. T.; Bolotin, K. I. Bandgap engineering of strained monolayer and bilayer MoS_2. *Nano Lett*. **2013**, *13*, 3626−3630.
22. Manzeli, S.; Allain, A.; Ghadimi, A.; Kis, A. Piezoresistivity and Strain-Induced Band Gap Tuning in Atomically Thin MoS_2. *Nano Lett*. **2015**, *15*, 5330–5335.
23. Choi, W.; Cho, M. Y.; Konar, A.; Lee, J. H.; Cha, G.-B.; Hong, S. C.; Kim, S.; Kim, J.; Jena, D.; Joo, J.; Kim, S. High-Detectivity Multilayer MoS_2 Phototransistors with Spectral Response from Ultraviolet to Infrared. *Adv. Mater*. **2012**, *24*, 5832−5836.
24. Zhang, W.; Huang, J.-K.; Chen, C.-H.; Chang, Y.-H.; Cheng, Y.-J.; Li, L.-J. High-Gain Phototransistors Based on a CVD MoS_2 Monolayer. *Adv. Mater*. **2013**, *25*, 3456−3461.
25. Lopez-Sanchez, O.; Lembke, D.; Kayci, M.; Radenovic, A.; Kis, A. Ultrasensitive photodetectors based on monolayer MoS_2. *Nat. Nanotechnol.* **2013**, *8*, 497−501.
26. Furchi, M. M.; Polyushkin, D. K.; Pospischil, A.; Mueller, T. Mechanisms of Photoconductivity in Atomically Thin MoS_2. *Nano Lett.* **2014**, *14*, 6165−6170.
27. Perea-López, N.; Lin, Z.; Pradhan, N. R.; Iñiguez-Rábago, A.; Laura Elías, A.; McCreary, A.; Lou, J.; Ajayan, P. M.; Terrones, H.; Balicas, L.; Terrones, M. CVD-grown

monolayered MoS_2 as an effective photosensor operating at low-voltage. *2D Mater*. **2014**, *1*, 011004.

28. Yin, Z.; Li, H.; Li, H.; Jiang, L.; Shi, Y.; Sun, Y.; Lu, G.; Zhang, Q.; Chen, X.; Zhang, H. Single-Layer MoS_2 Phototransistors. *ACS Nano* **2012**, *6*, 74−80.
29. Li, Z.; Chen, J.; Dhall, R.; Cronin, B.S. Highly efficient, high speed vertical photodiodes based on few-layer MoS_2. *2D Mater.* **2017**, *4*, 015004.
30. Kim, T.-Y.; Ha, J.; Cho, K.; Pak, J.; Seo, J.; Park, J.; Kim, J.-K.; Chung, S.; Hong, Y.; Lee, T. *Submitted*.

6. Summary

In this dissertation, I have dealt with the study on the transistors based on atomically thin MoS_2 semiconducting channel. Most of the chapters were devoted to analysis of the electrical characteristics of MoS_2 field-effect transistors. From the mechanically exfoliated MoS_2 samples to the CVD-synthesized large-area monolayer MoS_2 films, and from the Ti/Au electrodes designed by conventional e-beam lithography to the transparent and flexible PEDOT:PSS electrodes deposited by inkjet-printing techniques, several ways of practical application of atomically thin MoS_2 were introduced.

국문초록

대면적 단분자층 이황화 몰리브덴 박막 합성 및 전계효과 트랜지스터에의 응용

수 나노미터로 얇은 분자층 두께의 이차원 전이금속 다이칼코젠(transition-metal dichalcogenides: TMDCs) 물질은 좋은 전계효과 모빌리티와 조절 가능한 밴드갭 에너지를 가지고 있어서 차세대 반도체로 주목받고 있다. 여러 TMDC 물질 중에서도 이황화 몰리브덴(MoS_2)은 단분자층 두께에서 1.8 eV의 직접 밴드갭 에너지를 가지고 있다. 따라서 MoS_2를 나노일렉트로닉스에 이용하고자 많은 응용 연구가 이루어지고 있는데, MoS_2의 광학적, 전기적 특성을 활용하기 위해서는 균일하면서 대면적의 MoS_2 박막을 합성해야만 한다. 이를 위해 화학기상증착법(chemical vapor deposition: CVD)으로 균일하면서 대면적을 가지는 MoS_2 박막을 합성하는 연구가 활발히 진행되었다.

그런데 일반적인 MoS_2연구에서는 무기 전극이나 유전물질을 전사시키거나 포토리소그래피를 이용해서 디자인하는데, 이런 공정은 유연 소자에 활용되기 힘들다. 따라서 이차원 TMDC물질의 장점을 활용해서 투명하면서 유연한 2차원 일렉트로닉스를 구현하려면 저온, 대면적, 저비용 공정이 가능한 새로운 접근방법이 필요하다. 이에 본 학위 논문에서는 분자층 두께로 얇은 MoS_2를 기반으로 한 전계효과 트랜지스터(field-effect transistor: FET)를 위한 MoS_2 합성과 FET에의 응용에 관해 다루고자 한다.

첫째, MoS_2 FET에 10 MeV의 고에너지 양성자 빔을 조사했을 때의 효과에 대해 논하고자 한다. 다양한 도즈량에서 고에너지 양성자 빔 조사 전후의 전기 특성이 분석되었는데, 전기적 특성 변화는 양성자 빔 조사에 의해 생성된 트랩들–SiO_2층에 트랩된 양전하를 띄는 옥사이드 전하와 MoS_2/SiO_2 계면에 생성된 트랩–으로 설명했다.

둘째, CVD로 대면적 단분자층 MoS_2 박막을 합성하는 연구에 대해 논하고자 한다. CVD로 합성된 MoS_2 박막의 단분자층 여부를 원자현미경(atomic force microscopy: AFM), 라만(Raman), 광발광(photoluminescence) 스펙트럼분석으로 확인했다.

셋째, 합성된 대면적 단분자층 MoS_2 박막에 저비용 잉크젯 프린팅으로 올린 은(Ag) 전극을 이용해서 제작한 FET의 전기적 특성에 관해 논하고자 한다.

단분자층 MoS_2 박막은 CVD로 합성되었고, 전극은 저비용 드롭 온 디맨드(drop-on-demand) 잉크젯 프린팅 공정으로 마스크나 전처리 없이 제작되었다. 잉크젯 프린팅으로 제작한 소자의 전기적 특성은 기존의 통상적인 포토리소그라피나 전자빔 리소그라피로 제작한 FET와 비슷했다.

마지막으로 대면적 MoS_2 박막에 잉크젯 프린팅으로 제작한 투명하면서 휘어지는 포토트랜지스터에 대해 논하고자 한다. 유전체와 전극을 포함하는 모든 구성요소들을 투명하며 휘어지는 기판에 전사된 MoS_2 박막 위에 프린팅했다. 단분자층으로 얇은 MoS_2 박막에 소프트한 유기 전극이나 유전층을 프린팅해서 제작한 포토트랜지스터는 매우 투명하면서 높은 유연성을 보였다.

주요어: 이황화몰리브덴(MoS_2), 전계효과트랜지스터, 전기적 특성, 화학기상증착법

학번: **2013-30113**

감사의 글

포항을 떠나 관악산 기슭에서 지낸 시간이 벌써 10년이 넘었습니다. 익숙해진 관악산을 떠나 새로운 삶을 시작하려니 만감이 교차하는데, 많은 분의 도움으로 여기까지 올 수 있었기에 이 자리를 빌려 감사의 말씀 드립니다.

우선, 박사 과정 동안 지도해주신 이탁희 교수님께 감사드립니다. 제 결혼식 주례사에서 말씀하셨듯 항상 가족처럼 지도하고 이끌어주셔서 고맙습니다. 사회에 나가서는 지도교수님 이름이 부끄럽지 않게 제 위치에서 최선 다하겠습니다. 버클리 Yali's café의 뜨거운 햇볕 아래 인사드린 게 엊그제 같은데, 지난 2년간 형처럼 도와주신 정승준 교수님께도 정말 감사드립니다. 대학원 동기면서 전임 방장이었던 현학형도 고맙습니다. 곧 졸업할 텐데 꼭 원하는 곳으로 가서 연구 계속 이어가기를 바랍니다. 버클리 Addison street에서 6개월간 동고동락했던 영걸이, 졸업 축하하고 지금은 힘들지만 좀 더 고생하면 좋은 곳으로 원하는 연구 하러 갈 수 있을 거야. MoS_2 팀에서 큰 도움 받았던 경준이, 진수도 정말 고맙다. 무늬만 팀장인 내가 할 일을 둘이 워낙 잘해줘서 내가 편하게 졸업하네. 내가 편했던 만큼 둘이 고생 많았는데 성실하고 영리하기에 우리팀 잘 이끌어주리라 믿어. 재근이, 유리, 지원이는 각자 앞에 있는 일들 해결해서 박사 졸업 잘했으면 좋겠다. 다음 방장인 왕택아, 연구하느라 바쁠 텐데 잘 부탁할게. 유기팀의 대경, 영록, 우철이, 분자팀의 연식, 준우, 정민이도 힘든 대학원 시간 잘 견뎌내고 웃는 모습으로 졸업했으면 좋겠다. 방장일 하는데 많이 도와주셨던 국은경 누나도 고맙습니다. 실험하러 먼 길 왔다갔다하는 인호, 독일에 있는 동구형, 홍릉에 있는 진곤이, 미국에 있는 민미숙 박사님께도 감사의 말 전합니다. 만난 시간은 짧지만 강기훈 박사님, 안희범, 김재영 학생에게도 감사의 인사 드립니다.

30년간 물심양면 뒷바라지 해주신 부모님께도 감사드립니다. 멀리 있다는 핑계로 자주 찾아뵙지 못하고 항상 마음고생만 시켜드리는 큰아들, 이제는 사회에 나아가 가장으로서 제 몫 하겠습니다. 항상 제 걱정하시는 할머니, 멀리 가더라도 자주 찾아뵐 테니 앞으로도 건강히 오래오래 사세요. 못난 사위 항상 생각해주시는 장인, 장모님. 좀 멀어지더라도 자주 찾아뵙고 은규 고생시키지 않겠습니다. 직장생활 하느라 바쁜데 가정의 대소사 신경 많이 써줘서 고마운 동생 여영이랑 제수씨. 앞으로는 제가 많이 돕겠습니다. 완규, 진규 두 처남도 누나랑 매형 신경써줘서 고마워.

그리고 결혼한 지 얼마 안 돼서 우리 살 곳 마련하느라 바빴던 내 아내 은규, 이제는 가장으로서 내 몫 다 할 테니 옆에서 많이 응원해줘. 지금처럼만 우리 서로 사랑하고 아껴주자.

Thank you for your help professor Hong. I'm leaving with a good memory in Nanomag Lab. I hope you and Elisa have a good time in Korea for many years to come.

자주 연락 못 하는 나지만 항상 고맙게 맞아주는 어릴적 친구들인 용준이, 준호, 태준, 한솔, 충기, 해욱, 준형이도 고맙다. 힘든 대학원 생활 동안 22동, 56동에서 얘기를 나눴던 학부 동기들인 필광, 한빛, 현호, 선욱, 덕형이도 고맙다. 다들 조금만 더 고생해서 졸업하자. 급하게 축구할 때마다 힘이 돼준? 진우, 승엽이도 고마워. 이역만리? 버클리 생활에 큰 도움 준 향근형, 회사 입사에 많은 도움을 주신 다운형도 고맙습니다. 군 생활때부터 지금까지 연락하고 지내는 진이랑 대현형, 종수도 고마워. 제가 여기 적지 못한 다른 많은 분들께도 다시 한번 감사드립니다.

10년 동안 후회 없이 공부하고 뛰어놀 수 있어서 즐거웠습니다. 10년 동안의 지식과 경험으로 교만해지는 것이 아니라, 겸손하게 나눌 줄 아는 사람이 되도록 부단히 노력하겠습니다. 앞으로 행복할 때도 슬플 때도 있겠지만 제 주위에 항상 저를 아껴주고 사랑해주는 사람들이 있단 걸 잊지 않겠습니다.

고맙습니다!